PAPER

Multi-physics design optimization of structural battery

To cite this article: Reza Pejman *et al* 2021 *Multifunct. Mater.* **4** 024001

IOP Publishing Multifunct. Mater. 4 (2021) 024001 https://doi.org/10.1088/2399-7532/abf158

Multifunctional Materials

PAPER

Multi-physics design optimization of structural battery

Reza Pejman, Emin Caglan Kumbur and Ahmad Raeisi Najafi*

Department of Mechanical Engineering and Mechanics, Drexel University, Philadelphia, PA 19104, United States of America

* Author to whom any correspondence should be addressed.

E-mail: arn55@drexel.edu

RECEIVED
4 February 2021

ACCEPTED FOR PUBLICATION
24 March 2021

PUBLISHED
6 April 2021

Keywords: structural battery, multi-physics, Li-ion battery, design optimization, multifunctional material

Abstract

Structural battery composite is a new class of multifunctional lightweight materials with profound potential in harvesting electrical energy in the form of chemical energy, while simultaneously providing structural integrity to the system. In this study, we present a multi-physics design optimization framework for structural battery. The objective of the optimization framework is to change the geometrical features and material types of the constituents in a composite lamina to maximize the allowable charging current for a constant rate of charging. In this optimization framework, three sets of inequality constraints are defined to keep the structural battery lightweight, and make sure that the amount of induced stress and generated heat due to the intercalation process remains small. We have also considered several design parameters such as geometrical features of the composite lamina, volume fractions of fibers and $LiFePO_4$ particles, and material types of constituents. The proposed framework includes a gradient-based design optimization method with the ability to perform the optimization process under any source of uncertainty in the material properties, manufacturing process, operating conditions, etc. It also contains a Bayesian design optimization scheme to select the best candidate for the materials of the constituents in a structural battery. We also develop an analytical sensitivity analysis of several electrochemical/thermal/structural response metrics with respect to a few geometrical and material design parameters of a composite lamina. The results show that by using the proposed optimization framework, we are able to maximize the allowable charging current for a constant rate of charging in the optimized solution compared to the considered reference designs while satisfying all of the prescribed constraints. Furthermore, we increase the design reliability of structural battery by at least 45% compared to the deterministic optimized solution. Finally, we find the optimized material types for the fiber and matrix in a structural battery.

Nomenclature

Symbol	Description
L	Length of composite lamina
W	Width of composite lamina
δ	Thickness of composite lamina
C_f	Relative lithium-ion concentration in the fiber
t	Time
D_f	Diffusion coefficient
γ_1	Coefficient of intercalate activity
r_ζ	Radius of species ζ
c_0	Maximum possible concentration of lithium-ion inside the fiber
i	Local current density
F	Faraday's constant
I_f	Current in each fiber
I_{lam}	Current in the lamina
n_f	Number of fibers

C_{rate}	Time for charging/discharging of the battery
Γ_ζ	Electrochemical capacity of species ζ
m_ζ	Total mass of species ζ
δ_c	Thickness of coating
$\mathfrak{f}_\zeta$	Volume fraction of species ζ
E_{st}	Stored energy
E_{in}	Inflow energy
E_{out}	Outflow energy
E_{g}	Energy generation
R_ζ	Resistance of species ζ
T	Temperature
c_p^{avg}	Weighted average of specific heat
s_ζ	Ion conductivity of species ζ
$\mathfrak{N}_\zeta$	Number of concentric circles in species ζ
u	Displacement
ε	Strain
β	Swelling coefficient
E_ζ	Modulus of elasticity of species ζ
ν	Poisson's ratio
α_ζ	Coefficient of thermal expansion of species ζ
σ	Stress
K_ζ	Bulk modulus of species ζ
G_ζ	Shear modulus of species ζ
θ	Objective function
$\mathbf{d}$	Vector of design parameters
lb_j	Lower bound for the design parameter d_j
ub_j	Upper bound for the design parameter d_j
$\mathbf{g}$	Vector of inequality constraints
C	Elasticity tensor
$\boldsymbol{\xi}$	Vector of random variables
$Y(\boldsymbol{\xi})$	Response function
r_i	PC coefficient
ψ_i	Polynomial basis functions
N_t	Total number of coefficients in the PCE
$E[.]$	Mathematical expectation
$\boldsymbol{\xi}^{(q)}$	Quadrature points
$\rho(\boldsymbol{\xi})$	Probability density function of the independent random variable
$w^{(q)}$	Weight of quadrature points
n_q	Number of quadrature points
$\mathfrak{A}$	Probability space
C_θ	Level of variability
Std	Standard deviation
n_g	Number of constraints
$\mathfrak{P}$	Level of reliability
P_f	Probability of failure
H	Heaviside function
n_{samples}	Number of Monte Carlo samples
T_{ref}	Reference temperature
V_ζ	Volume of species ζ

1. Introduction

One of the major hindering factors in the development of electric vehicles is that the specific energy of the batteries is low. To put it in illustration, as it is shown in figure 1(a), the share of battery in the total mass of a typical electric vehicle such as Tesla Model S is about 28.6%, while the share of mass for the source of energy (fuel) in a fairly common gasoline car such as Honda Civic is only about 3.3% [1]. Thus, this is a critical issue for designers that are trying to make electric vehicles as efficient and lightweight as possible. There are two different approaches to tackle this problem. One approach is enhancing the specific energy of batteries as most of the research groups are currently working on. An alternative approach that we are looking into in this study is to take advantage of multifunctional materials enabling us to combine several functions [2–11], which can potentially lead to a significant reduction in the mass of electric vehicles as it is discussed in [12].

Recently, a class of fiber-reinforced composite (FRC) materials, namely structural battery composites (SBCs) is developed, with the ability to harvest electrical energy in the form of chemical energy while simultaneously provides mechanical integrity in a structural system [13–20]. For instance, as it is shown in figure 1(b), SBC can be introduced in different parts of an electric vehicle, e.g. doors, hood, roof, etc. And as it is discussed in [12], introducing SBC in electric vehicles has the potential to reduce both the mass of vehicle's structure and the required amount of battery for that vehicle. These materials are quite promising, but they are still in their early stages of development, and further studies are required for their advancements. The need to fulfill multifunctionality in SBC results in intrinsically conflicting physical property demands. SBC simultaneously requires to provide mechanical integrity and harvest electrical energy, which in general can be conflicting demands [21]. Moreover, electrochemical cyclings generate heat and we need to protect the SBC from overheating. The design of SBC plays a key role in creating a trade-off between these conflicting physical property demands. Thus, one of the most important areas of research on SBC is developing a rigorous multi-physics design optimization approaches, as it is the topic of our current study.

There are two different general designs for SBC (a) laminated [13, 15, 18] and (b) three-dimensional (3D) [19, 20] battery architecture. In the laminated battery, each lamina has a different function. They serve as electrodes, separators, or collectors. In 3D battery architecture, carbon fibers are used as both negative electrode and reinforcement. Moreover, each carbon fiber is coated with a lithium-ion conductive and electrically insulating solid polymer electrolyte, which works as both electrolyte and separator layer. By adding a specific type of particles (e.g. $LiFePO_4$) to the polymer matrix, it is possible to make it a positive electrode in the battery cell. We concentrate on 3D battery structure in this study as schematically shown in figure 1(c).

A multi-physic model is required to model the mechanical, thermal, and electrochemical processes that happen during the charging and discharging of SBC. Several studies are presented in the literature on modeling the internal stresses in SBC due to electrochemical cyclings [22–26]. There are also few studies on modeling the damage induces by these internal stresses [27–29]. Moreover, Carlstedt *et al* performed a parametric study on the effects of the state of charge on the elastic properties of 3D structural battery composites [30]. However, these studies did not consider the thermal process that occurs in SBC. Carlstedt *et al* recently addressed this issue by presenting a semi-analytic approach to model the mechanical, thermal, and electrochemical processes under the galvanostatic condition (i.e. constant current charge/discharge cycles) in a structural battery [31].

There are very few studies in the literature on presenting a design optimization framework for SBC [21]. As one of the few studies in this area, Lee *et al* proposed a multi-objective topology optimization approach to optimize the microstructure of a structural battery electrolyte. They found the material distribution of the structural battery electrolyte that maximize ionic conductivity and minimize compliance. However, their approach only considers structural electrolyte instead of the entire structural battery. Thus, there is an absolute need in the literature to present a multi-physics design optimization framework for SBC. Asp and Greenhalgh in their recent book chapter [32] mentioned the lack of enough studies in the literature on the design aspect of SBC.

In this study, we consider a structural battery that includes carbon fibers coated with poly(methoxy polyethylene glycol (350) monomethacrylate) and bi-continuous polymer matrix reinforced with $LiFePO_4$ and carbon black (CB) particles. Our goal is to provide a design optimization framework for a structural battery. We aim to maximize the allowable charging current for a constant rate of charging within the structural battery while three sets of inequality constraints are defined on the maximum allowable mass, temperature, and stress in a structural battery (see figure 1(e)). In the proposed optimization framework, we consider several design parameters such as geometrical features of the composite lamina (length, width, and thickness of composite lamina, and thickness of coating), volume fractions of fibers and $LiFePO_4$ particles, and material types of fiber and matrix.

Various design optimization methodologies can be used to optimize the material and geometrical features of a structural battery such as gradient-based and non-gradient-based approaches. In this study, we use the gradient-based design optimization method to optimize the geometrical features of a structural battery. Note that the gradient-based design optimization method is a widely-used approach in the design community [33–36]. There are also various methods that we can use to optimize the type of materials for the constituents in a structural battery. Among them, we select the Bayesian design optimization approach, which is a non-gradient based method. Bayesian design optimization approach shows promising potential for the optimization problems dealing with categorical design variables such as material type.

We also want the proposed optimization framework to be able to consider any sources of uncertainty in the material properties, geometrical features, operating conditions, etc during the optimization process. The presence of uncertainty may result in a substantial deviation in the structural battery performance and can potentially lead to a system failure. Hence, considering uncertainty during the design optimization process

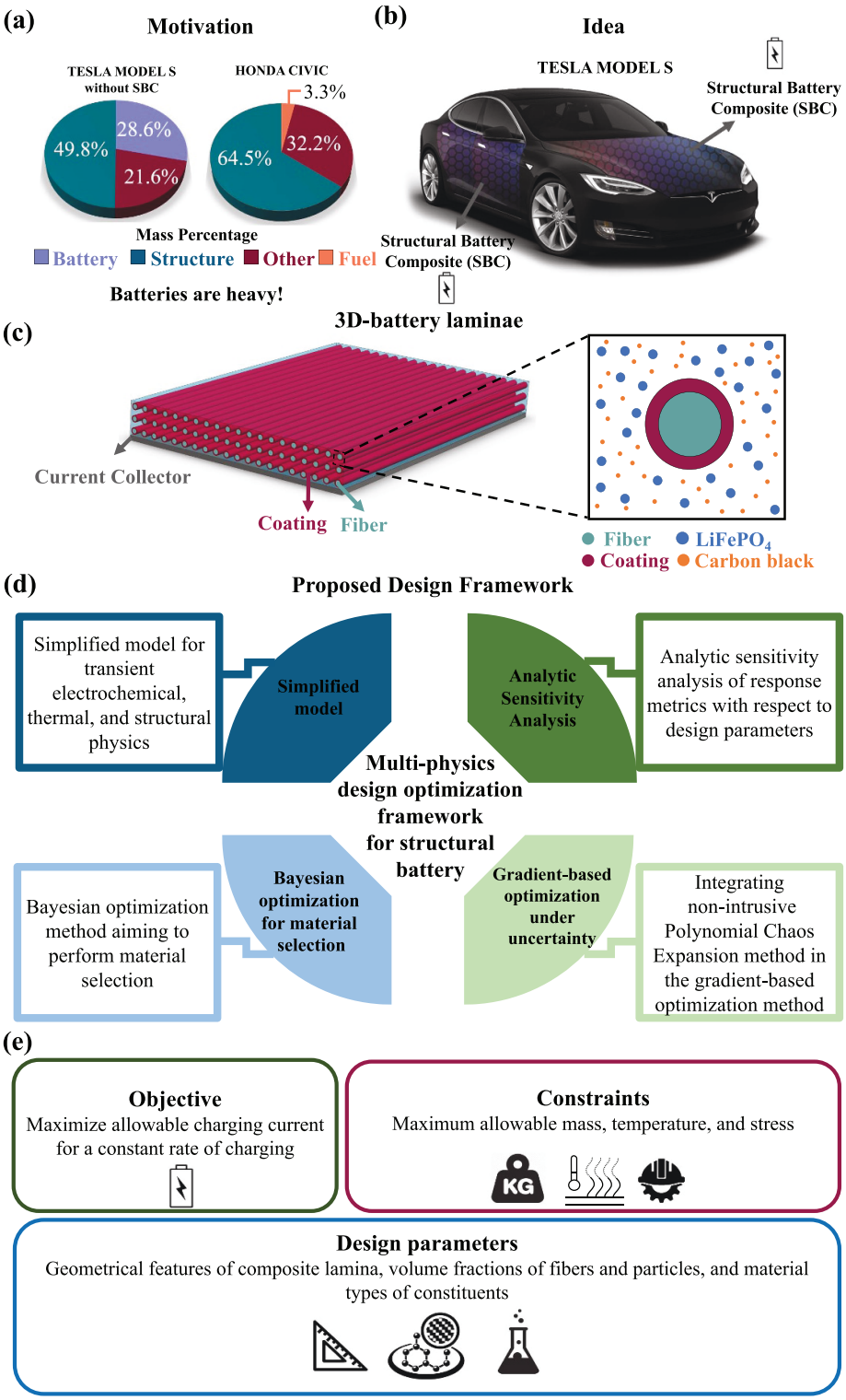

Figure 1. (a) Motivation: specific energy of the batteries is low. A comparison between the share of the source of energy in the mass of a typical electric vehicle such as Tesla Model S and a regular gasoline car such as Honda Civic, (b) idea: introducing structural batteries in different parts of electric vehicles to reduce the vehicle's mass and the required amount of battery for an electric vehicle, (c) schematic of a 3D-battery lamina, (d) proposed design optimization framework for structural battery in this study, and (e) objective function, constraints, and design parameters considered in this study.

enables the designers to produce a reliable design, i.e. a design that satisfies the prescribed constraints even in the presence of uncertainty in the material properties, manufacturing process, operating conditions, etc for structural batteries. There are various approaches to integrate uncertainty into a design optimization process, such as local expansion-based methods [37], simulation-based methods [38–41], most probable point-based methods [42, 43], functional expansion-based methods [44–47], etc. The method of choice for this study is the non-intrusive polynomial chaos expansion (PCE) approach, which is one of the members of functional

expansion-based methods. We select this approach due to its fast convergence property, and its easy implementation process. Indeed, the non-intrusive PCE method treats the simulation model as a black-box, and we do not need to perform any modification to the existing deterministic approach.

The four parts of the proposed design optimization framework are shown in figure 1(d). To develop the gradient-based design optimization part of the framework, we perform an analytic sensitivity analysis of several response metrics such as the amount of produced charging current, temperature, mass, and stress in the structural battery with respect to a few important design parameters such as length, width, and thickness of composite, the volume fraction of positive electrode particles, the volume fraction of negative electrodes, and also coating thickness. We then combine the gradient-based design optimization framework with the non-intrusive PCE method to incorporate uncertainty. The non-intrusive nature of the proposed approach allows for almost any source of uncertainty to be included virtually in the design optimization procedure. For uncertainty quantification, we use the reliability-based design optimization (RBDO) method, in which the main goal is producing a reliable design for a structural battery. By reliable design, we mean that we aim to decrease the variation in the performance of the structural battery under different sources of uncertainty. In this method, we efficiently and accurately approximate the statistical moments, failure probabilities, and their sensitivities with respect to the design variables.

For the Bayesian design optimization scheme, we consider the material types of the polymer matrix and fibers in addition to the volume fractions of positive electrode particles and negative electrodes as the design parameters. Thus, we have both quantitative and qualitative design parameters. Bayesian optimization is a global optimization approach in which a Gaussian process model is maintained for the objective function, and the objective values are constantly being used to train the model [48].

The remainder of the paper is organized as follows: section 2 presents a multi-physics model for a structural battery. In section 3, we propose the design optimization approaches and we develop the sensitivity analysis of the response metrics with respect to the design parameters. In the last section, we solve several numerical problems to highlight the unique features of the proposed framework, and we provide some physical interpretation and discussions to give insights for the designers regarding the design of a structural battery.

2. Multi-physics model

The core of this study is design optimization, which is an iterative process. Using a high fidelity model to account for all of the complexity of a problem comes at the price of a high computational cost. Thus, using a simplified or reduced-order model is a priority in most design optimization studies [21]. In particular, in this study, we are interested in performing a transient study[1] on a multi-physics problem for the design optimization of structural battery, which is a costly problem to solve. Thus, using a simplified model is quite essential for us. Recently, a new semi-analytical multi-physics model is proposed and verified for structural battery in [31]. They simplified the general multi-physics problem, which involves multiple coupled physical phenomena, to develop a practical model for determining the internal stress state of the structural battery during electrochemical cycling. In this study, we use the same model, but we slightly modify the way that we solve the thermal and structural modules. For completeness, we provide the key concepts and notations regarding this model in this section.

The schematic of the problem setup is shown in figure 2. A thin composite lamina with length (L), width (W), and thickness (δ) is considered. This structural battery follows the same technology as their conventional lithium-ion batteries: matrix works as the cathode (positive electrode) and fibers as the anode (negative electrode), and fiber coating plays two roles (a) separator layer and (b) electrolyte. During the charging, lithium-ions shuttle from the cathode to the anode, leading to creating an electrical potential difference between the electrodes. The opposite reactions during the discharging enable the battery to deliver electrical power. Charging and discharging of structural battery causing volume changes in the electrodes as well as generating heat in the structure. As a result, internal stress will be induced in the structural battery. The objective of this multi-physics model is to predict the amount of induced stress, temperature change, and lithium concentration change in the constituents during the charging cycles.

In this study, IMS65 and T800 carbon fibers are considered as the possible options to be used in the structural battery. These intermediate modulus fibers have demonstrated very high electrochemical capacities, which makes them a perfect choice for structural batteries. Fiber coatings are assumed to be made of poly(methoxy polyethylene glycol (350) monomethacrylate) developed in [49]. Matrix is considered to be made of bi-continuous polymer network proposed in [50]. Three bi-continuous polymers with different

[1] Note that the battery is inherently a transient operating device, therefore we are required to perform a transient analysis on the multi-physics problems solved in this study.

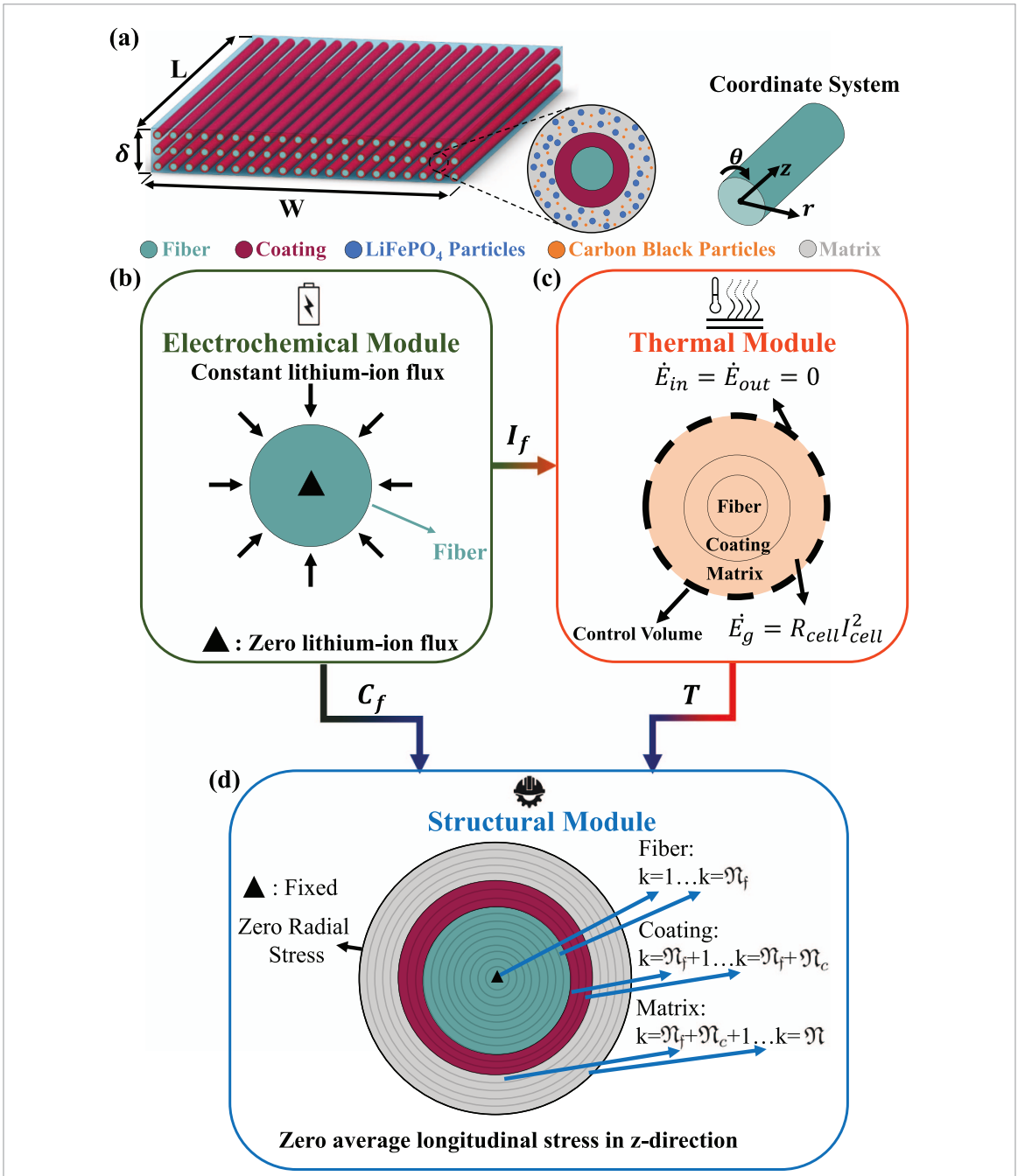

Figure 2. (a) Schematic of structural battery lamina. Problem setups for (b) electrochemical, (c) thermal, and (d) structural modules.

Table 1. Chemical composition of matrix polymers.

Sample	A (g)	B (g)	1.0 M LiTFS in EC : DMMP (g)	DMPA (g)
A/0.65	1	0	0.65	0.01
AB/0.65	0.5	0.5	0.65	0.01
B/0.65	0	1	0.65	0.01

compositions are considered in this study and they are listed in table 1. The main components of these polymers are bisphenol A dimethacrylate (A), bisphenol A ethoxylate dimethacrylate (B), dimethyl methylphosphonate (97%) (DMMP), ethylene carbonate (99% anhydrous) (EC), 2,2-Dimethoxy-2-phenylacetophenone (DMPA), and lithium trifluoromethanesulfonate (LiTFS) (96%) [50]. Matrix is reinforced with $LiFePO_4$ and carbon black (CB) particles.

The key assumptions of the multi-physics model used in this study are summarized as follows: (a) galvanostatic cycling is assumed, i.e. constant current charge cycles; (b) perfect adhesion is assumed between

fiber and coating as well as between the coating and matrix; (c) fibers are assumed to be transversely isotropic, and coatings and matrix are considered to be isotropic; (d) small deformation is assumed, enabling us to use linear elasticity; (e) the analysis is assumed to be one-way, i.e. the model only considers the effect of volume changes and heat generation on stresses[2]; (f) the amount of generated heat within a structural battery due to electrochemical cycling is assumed to be dominated by ohmic heat; and (g) as it has been assumed in the previous studies [24, 28, 31], this model considers the diffusion coefficient of fiber to be constant during electrochemical cycling for simplicity. Similar to the previous studies [31], one of the limitations of this model is related to not considering the mass transport in the electrolyte. In the future studies, we aim to extend the model to account for this limitation.

Three physics of structural, thermal, and electrochemical are involved in this problem. In sections 2.1–2.3, we discuss the governing equations and the proposed solutions for each one of these physics.

2.1. Electrochemical module

In this section, we solve the governing equation associated with the electrochemical module. We consider a cylindrical coordinate, where r is the radial coordinate, θ is the angular (hoop) coordinate, and z is the longitudinal coordinate as shown in figure 2(a). Lithium-ions diffuse into each fiber during the intercalation process, and the change in the relative lithium concentration of the fiber can be described by the Fick's second law of diffusion,

$$\frac{\partial C_{\mathrm{f}}}{\partial t} = D_{\mathrm{f}} \nabla^2 C_{\mathrm{f}}, \tag{1}$$

where C_{f} is the relative lithium-ion concentration in the fiber, t is time, D_{f} is the diffusion coefficient, and ∇^2 is the Laplace operator. Since the length of fibers in the z-direction are much larger than the other characteristic dimensions of fiber, the diffusion can be considered in-plane, i.e. only function of r and θ. Moreover, if the fiber is undamaged, the lithium-ion concentration in the fiber does not change in the θ direction, thus, the Laplace term becomes $\nabla^2 = \frac{1}{r}\frac{\partial}{\partial r}\left(r\frac{\partial}{\partial r}\right)$.

The problem setup for the electrochemical module is shown in figure 2(b). To solve (1), two boundary conditions and one initial condition are needed. For the initial condition, we assume that at time zero, the lithium concentration in the fiber is zero,

$$C_f(r, t = 0) = 0. \tag{2}$$

For the first boundary condition, we consider a zero lithium-ion flux at the fiber's center,

$$\nabla C_f(r = 0, t) = 0, \tag{3}$$

where ∇ is the gradient operator (i.e. $\nabla = \frac{\partial}{\partial r}$). To present the second boundary condition, we need to consider one more assumption, in which, we neglect the lithium-lithium interactions inside the fiber leading to approximation $\frac{d(\ln\gamma_1)}{d(\ln C_f)} \approx 0$, where γ_1 is the coefficient of intercalate activity. Under this assumption, the second boundary condition can be written as [28, 52, 53]

$$-D_{\mathrm{f}} c_0 \nabla C_{\mathrm{f}}(r = r_{\mathrm{f}}, t) = \frac{i}{F}, \tag{4}$$

where r_{f} is the fiber radius, c_0 is the maximum possible concentration of lithium-ion inside the fiber, i is the local current density, and F is the Faraday's constant. Local current density can be computed as $i = I_{\mathrm{f}}/(2\pi r_{\mathrm{f}} L)$, where I_{f} is the current in each fiber and $2\pi r_{\mathrm{f}} L$ is the circumferential area of fiber. The current in each fiber is equal to $I_{\mathrm{f}} = I_{\mathrm{lam}}/n_{\mathrm{f}}$, where I_{lam} is the amount of current in the lamina and n_{f} is the number of fibers. The amount of current in the lamina can be computed as follows:

$$I_{\mathrm{lam}} = \min\{\ _{\mathrm{f}} m_{\mathrm{f}},\ _{\mathrm{p}} m_{\mathrm{p}}\} C_{\mathrm{rate}}, \tag{5}$$

where C_{rate} is the time for charging/discharging of the battery and $_{\mathrm{f}}$ and $_{\mathrm{p}}$ are electrochemical capacities of fiber and particle, respectively. m_{f} and m_{p} are the total mass of fibers and particles within the matrix, respectively. An analytical solution for (1)–(4) is provided in [54] and can be written as

$$C_{\mathrm{f}}(r, t) = \left(\frac{i r_{\mathrm{f}}}{c_0 D_{\mathrm{f}} F}\right) \left(-0.25 : \frac{2 D_{\mathrm{f}} t}{r_{\mathrm{f}}^2} : \frac{r^2}{2} - 2\prod_{n=1}^{\infty} \frac{J_0(\lambda_n r)}{\lambda_n^2 J_0(\lambda_n)} \exp\right) \frac{-D_{\mathrm{f}} t \lambda_n^2}{r_{\mathrm{f}}^2}\left(\right), \tag{6}$$

[2] Indeed, based on the experimental observations in [51], the model assumes that mechanical stresses would not affect the electrochemical capacity and current flow within the battery cell.

where $\mathfrak{r} = r/r_f$, r is the radial distance from the fiber's center, J_0 is the zero-order Bessel's function of the first kind, and λ_n is the nth root of $J_1(\lambda)$.

2.2. Thermal module

In the thermal module, we use a one-dimensional heat generation model based on the thermal energy balance. The problem setup is shown in figure 2(c). We write the thermal energy balance for each cell that consists of one fiber, it is coating, and it is surrounding matrix. The radius of the coating (r_c) is equal to the summation of the radius of fiber (r_f) and the thickness of coating (δ_c). And the radius of matrix (r_m) can be computed as $r_m = r_f/\sqrt{\mathfrak{f}_f}$ where $\mathfrak{f}_f$ is the fiber volume fraction in the lamina. We consider a control volume around this cell, so the first law of thermodynamic can be written as:

$$\frac{\partial E_{st}}{\partial t} = \frac{\partial E_{in}}{\partial t} - \frac{\partial E_{out}}{\partial t} + \frac{\partial E_g}{\partial t}, \tag{7}$$

where E_{st} is the stored energy, E_g is the energy generation, and E_{in} and E_{out} are inflow and outflow terms of energy transport across the control surfaces.

In terms of boundary conditions, we assume an adiabatic heat transfer condition for structural battery lamina and its surroundings, i.e. ($\partial E_{in}/\partial t = 0$ and $\partial E_{out}/\partial t = 0$). This assumption is motivated by the fact that the amount of heat generated by each cell is the same and since the thermal conductivity of the surrounding polymer matrix is low, the amount of heat transfer between the cells is very small [31]. Moreover, each laminae will be stacked in a laminate, and they need to be protected against moisture and oxygen. Thus, further insulation will be required in the final application. As a result, the heat transfer between the battery cells and the surrounding will be further limited.

The second boundary condition is the presence of an ohmic heat generation rate. Under the assumption that Ohm's law is applicable, the ohmic heat generation rate can be computed as $\partial Q_{ohm}/\partial t = R_{cell} I_{cell}^2$, where R_{cell} and I_{cell} are the resistance and current of the cell, respectively. We assume that the chemical reactions heat generation rates are negligible in comparison with the ohmic heat generation rate. Hence, $\partial E_g/\partial t = R_{cell} I_{cell}^2$. Equation (7) can be simplified as follows for the thermal response of each cell

$$m_{cell} c_p^{avg} \frac{\partial T}{\partial t} = R_{cell} I_{cell}^2, \tag{8}$$

where m_{cell} is the mass of the cell, T is the temperature, and c_p^{avg} is the weighted average of specific heat and can be calculated as

$$c_p^{avg} = \frac{1}{m_{tot}} \prod_{n=1}^{5} m_n c_{p_n}, \tag{9}$$

where m_{tot} is the total mass, and n corresponds to the nth phase (fiber, coating, matrix, $LiFeP_4$ particles, and carbon black particles).

R_{cell} can be computed as the sum of the resistance of the paths in the fiber (R_f), coating (R_c), matrix (R_m), and carbon black particles (R_{cb}). These resistances are given by the following equations[3],

$$R_f = \frac{L}{2\pi r_f^2 s_f}, \tag{10}$$

$$R_c = \frac{\ln(r_c/r_f)}{2\pi L s_c}, \tag{11}$$

$$R_m = \frac{\ln(r_c + 0.5 r_m - r_c)/r_c}{2\pi L s_m}, \tag{12}$$

$$R_{cb} = \frac{\delta}{2 r_m L s_{cb}}, \tag{13}$$

where s_c and s_m are the ion conductivity of the coating and matrix, respectively, and s_f and s_{cb} are the electrical conductivity of the fiber and carbon black particles, respectively. The variation of resistances due to volume changes during charging is assumed to be negligible. Note that as it is shown in [50], s_c and s_m are a

[3] For further details regarding derivation of resistances in the constituents, readers are referred to [31].

function of temperature. We will present the respective equations of them for materials used in this study in section 4. Hence, R_{cell} is a function of temperature. We rearrange (8) as

$$\int_{T_j}^{T_{j+1}} \frac{dT}{R_{\text{cell}}} = \frac{I_{\text{cell}}^2)t_{j+1} - t_j}{m_{\text{cell}}c_p^{\text{avg}}}, \tag{14}$$

where j corresponds to the time step j. This is a nonlinear equation, and we solved it by taking advantage of *fzero* function in MATLAB [48].

2.3. Structural module

The problem setup for the structural module is shown in figure 2(d). We aim to find the stress distributions in the fiber, coating, and matrix caused by heat generation and volume change of constituents. We consider the same cell as the one described in section 2.2, which contains a fiber, it is coating, and it is surrounded matrix. This axisymmetric problem has a semi-analytical solution by using the concentric cylinder (CC) model proposed in [30, 55]. As it is shown in figure 2(d), we divide the constituents into ($\mathfrak{N}$ = $\mathfrak{N}_f$: $\mathfrak{N}_c$: $\mathfrak{N}_m$) concentric circles, where $\mathfrak{N}_f$, $\mathfrak{N}_c$, and $\mathfrak{N}_m$ are the number of concentric circles in fiber, coating, and matrix, respectively.

Navier equation for axisymmetric problem ($\mathbf{u}$ = u_r)r+$\mathbf{e_r}$) can be written as [56]

$$\frac{d^2u_r}{dr^2} : \frac{1}{r}\frac{du_r}{dr} - \frac{u_r}{r^2} = 0, \tag{15}$$

where $\mathbf{e_r}$ is the unit vector in radial direction and u_r is the radial displacement. The solution of (15) for each concentric circle k can be written as

$$u_r^k = A_1^k r : \frac{A_2^k}{r}, \tag{16}$$

where A_1^k and A_2^k are constants to be determined for each concentric circle $k \in]1, \mathfrak{N}$.

The strain-displacement relations are given by

$$\varepsilon_r^k = \frac{\partial u_r^k}{\partial r}, \qquad \varepsilon_\theta^k = \frac{u_r^k}{r}, \tag{17}$$

where ε_r^k and ε_θ^k are radial and hoop strains for each concentric circle k, respectively. Generalized plain strain condition is assumed for this problem, i.e. ε_z = ε_{z0} = const.

The fibers are assumed to be transversely isotropic, and the coatings and matrix are considered to be isotropic. Hook's law for fibers ($k \in]1, \mathfrak{N}_{\text{f}}$) can be written as

$$\varepsilon_r^k - \beta_r^k C_f^k - \alpha_r^{k-} T^k = \frac{1}{E_r^k}\sigma_r^k - \frac{\nu_{r\theta}^k}{E_r^k}\sigma_\theta^k - \frac{\nu_{zr}^k}{E_z^k}\sigma_z^k, \tag{18}$$

$$\varepsilon_\theta^k - \beta_\theta^k C_f^k - \alpha_\theta^{k-} T^k = \frac{1}{E_r^k}\sigma_\theta^k - \frac{\nu_{r\theta}^k}{E_r^k}\sigma_r^k - \frac{\nu_{zr}^k}{E_z^k}\sigma_z^k, \tag{19}$$

$$\varepsilon_z^k - \beta_z^k C_f^k - \alpha_z^{k-} T^k = \frac{1}{E_z^k}\sigma_z^k - \frac{\nu_{zr}^k}{E_r^k}\sigma_r^k - \frac{\nu_{zr}^k}{E_r^k}\sigma_\theta^k, \tag{20}$$

where β_r^k, β_θ^k, and β_z^k are the swelling coefficients of fiber in the radial, hoop, and longitudinal directions for concentric circle k, respectively. E_r^k and E_z^k are the radial and longitudinal modulus of elasticity of concentric circle k. Poisson's ratio in $r\theta$ and zr planes are shown with $\nu_{r\theta}$ and ν_{zr}, respectively. α_r^k, α_θ^k, and α_z^k are the coefficients of thermal expansion in the radial, hoop, and longitudinal directions for concentric circle k, respectively. $^-$ T is temperature change, and σ_r, σ_θ, and σ_z are the components of stress in radial, hoop, and longitudinal directions, respectively.

We can write the Hook's law for coatings and matrix as follows ($k \in]\mathfrak{N}_{\text{f}}$: 1, $\mathfrak{N}$):

$$\varepsilon_r^k - \alpha_r^{k-} T^k = \frac{1}{E^k})\sigma_r^k - \nu^k)\sigma_\theta^k : \sigma_z^k +, \tag{21}$$

$$\varepsilon_\theta^k - \alpha_\theta^{k-} T^k = \frac{1}{E^k})\sigma_\theta^k - \nu^k)\sigma_r^k : \sigma_z^k +, \tag{22}$$

$$\varepsilon_z^k - \alpha_z^{k-} \; T^k \; [\; \frac{1}{E^k})\sigma_z^k - \nu^k)\sigma_r^k : \; \sigma_\theta^k +\!+ \tag{23}$$

In order to solve these equations and find the stress, strain, and displacement components, we need to find $2\mathfrak{N} : \; 1$ unknowns, which includes $\mathfrak{N}$ values for A_1^k, $\mathfrak{N}$ values for A_2^k, and the constant ε_{z0}. Hence, we need $2\mathfrak{N} : \; 1$ boundary conditions. For the first boundary condition, we can consider a zero displacement at the symmetry axis of the fiber,

$$u_r^1)r \; [\; 0 +\![\; 0. \tag{24}$$

Continuity needs to be satisfied on the interfaces between the concentric circles for displacement and stress, which provides $2\mathfrak{N} - 2$ equations,

$$u_r^k)r_k +\![\; u_r^{k+1})r_k +\!, \quad \sigma_r^k)r_k +\![\; \sigma_r^{k+1})r_k +\! \tag{25}$$

The outer boundary is considered to have a zero radial stress,

$$\sigma_r^{\mathfrak{N}})r_{\mathfrak{N}} +\![\; 0. \tag{26}$$

Since generalized plain strain is assumed, the strain in the longitudinal direction needs to result in a zero average longitudinal stress in the same direction,

$$\sigma_z^{\text{avg}} \; [\; \frac{2}{r_{\mathfrak{N}}^2} \prod_{k=1}^{\mathfrak{N}} \int_{r_{k-1}}^{r_k} r\sigma_z dr \; [\; 0. \tag{27}$$

Hence, we have $2\mathfrak{N} : \; 1$ unknowns and $2\mathfrak{N} : \; 1$ equations. This system of equations can be written as

$$\mathbf{Ax} \; [\; \mathbf{b}, \tag{28}$$

where $\mathbf{A}$ is the matrix of coefficients with dimension $)2\mathfrak{N} : \; 1 \times 2\mathfrak{N} : \; 1 +\!, \mathbf{x}$ is the vector of unknowns including A_1^k, A_2^k, and ε_{z0} for $k \in]1, \mathfrak{N}$ with dimension $)2\mathfrak{N} : \; 1 \times 1 +\!,$ and $\mathbf{b}$ is the vector of known values with dimension $)2\mathfrak{N} : \; 1 \times 1 +\!$

We should also emphasize that in the computation of (21)–(23) for the particle reinforced matrix, we need to use the effective thermal expansion coefficient ($\alpha_{m,\text{eff}}$) and effective modulus of elasticity ($E_{m,\text{eff}}$) as suggested in [57, 58]

$$\alpha_{m,\text{eff}} \; [\; \alpha_\text{p} \mathfrak{f}_\text{p} : \; \alpha_m)1 - \mathfrak{f}_\text{p} +\!: \; \frac{\alpha_\text{p} - \alpha_m}{\frac{1}{K_\text{p}} - \frac{1}{K_m}} \Big) \frac{1}{K_{m,\text{eff}}} - \Big) \frac{\mathfrak{f}_\text{p}}{K_\text{p}} : \; \frac{1 - \mathfrak{f}_\text{p}}{K_m} \Big(\Big(, \tag{29}$$

$$E_{m,\text{eff}} \; [\; \frac{9K_{m,\text{eff}}G_{m,\text{eff}}}{3K_{m,\text{eff}} : \; G_{m,\text{eff}}}, \tag{30}$$

where $\mathfrak{f}_\text{p}$ is the volume fraction of particles within the matrix. α_m and α_p are the thermal expansion coefficient of matrix and particle, respectively. K_m and K_p are the bulk modulus of matrix and particle, respectively. $K_{m,\text{eff}}$ is the effective bulk modulus and it can be computed as

$$K_{m,\text{eff}} \; [\; K_m : \; \frac{)K_\text{p} - K_m +\!)3K_m : \; 4G_m +\!\mathfrak{f}_\text{p}}{3K_\text{p} : \; 4G_m - 3)K_\text{p} - K_m +\!\mathfrak{f}_\text{p}}, \tag{31}$$

and $G_{m,\text{eff}}$ is the effective shear modulus given by

$$G_{m,\text{eff}} \; [\; G_m : \; \frac{\mathfrak{f}_\text{p}}{\frac{1}{G_\text{p} - G_m} : \; \frac{6(1-\mathfrak{f}_\text{p})(K_m + 2G_m)}{5G_m(3K_m + 4G_m)}}, \tag{32}$$

where G_m and G_p are the shear modulus of matrix and particle, respectively. We verify the presented multi-physics analysis module by comparing the results of our code with COMSOL in appendix A.

3. Design optimization frameworks

The proposed design optimization framework can perform (a) deterministic gradient-based optimization, (b) gradient-based design optimization under uncertainty, and (c) Bayesian optimization. The flow chart showing the steps in each one of these three schemes is shown in figure 3. In sections 3.1–3.3, the details of the steps in each one of these schemes are presented.

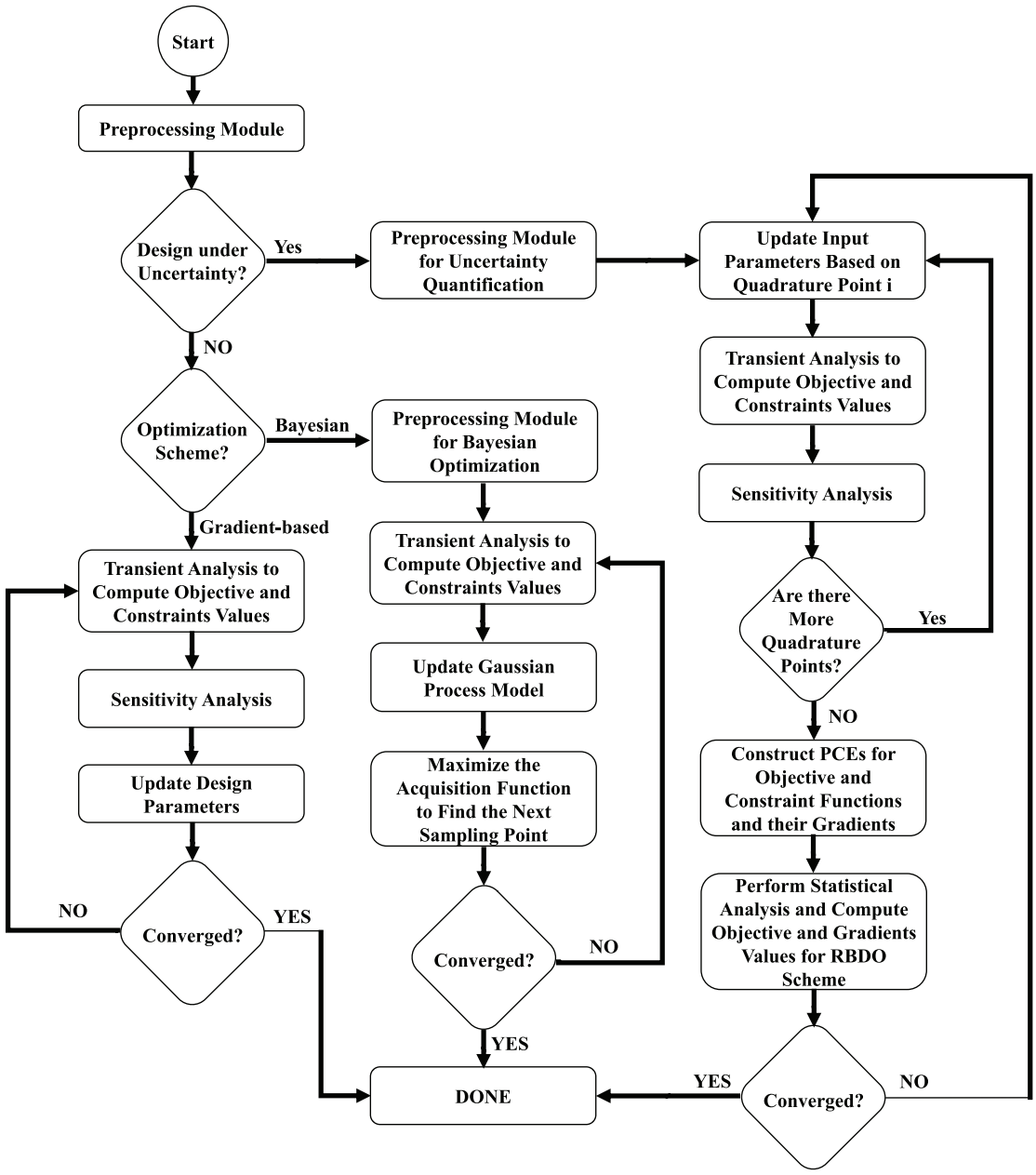

Figure 3. Flow chart of the proposed design optimization framework in this study.

3.1. Gradient-based design optimization

A deterministic design optimization problem can be formulated as

$$\begin{aligned} &\min_{\mathbf{d}} \theta, \\ &\text{such that } lb_j \leqslant d_j \leqslant ub_j, \quad j = 1, 2, \ldots, n_d \\ &\mathbf{g} \leqslant \mathbf{0}, \end{aligned} \tag{33}$$

where θ is the objective function, $\mathbf{d}$ is the vector of design parameters, lb_j and ub_j are the lower and upper bounds for the design parameter d_j, respectively, and $\mathbf{g}$ is the vector of inequality constraints. In this study, the objective is to maximize the allowable charging current (I_{lam}) for a constant rate of charging (minimize $-I_{\text{lam}}$) while there are constraints on the maximum value of mass, generated temperature, and induced stress in the battery.

In this scheme, we perform an analytic sensitivity analysis of the objective function and constraints with respect to the design parameters. Six different quantitative design parameters are considered for this scheme, including length, width, and thickness of structural battery, the thickness of coating, volume fraction of fiber,

and volume fraction of particles within the matrix. We have also considered four response metrics of current, mass, stress, and temperature.

The sensitivity of current and mass with respect to any of the design parameters can explicitly be found. Here, we present the sensitivity of the stress with respect to design parameter d_j. Without loss of generality, we can write Hook's law for the component p of the stress vector for the concentric circle k at the end of the charging process as

$$\sigma_p{}^k \; [\;\; C_{pq}{}^k \varepsilon_q{}^k, \tag{34}$$

where C is elasticity tensor. For conciseness, we show (34) as $\sigma \; [\;\; \mathbf{C}\boldsymbol{\varepsilon}$.

Taking the derivative of equation (34) with respect to the design variable d_j yields

$$\begin{aligned} \frac{d\sigma}{dd_j} \; [\;\; & \frac{\partial \mathbf{C})E)T)d_j + C_f)d_j + + +}{\partial d_j} \boldsymbol{\varepsilon})x)d_j + \alpha)d_j + C_f)d_j + T)d_j + + \\ & : \;\; \mathbf{C})E)T)d_j + C_f)d_j + + + \frac{\partial \boldsymbol{\varepsilon})x)d_j + \alpha)d_j + C_f)d_j + T)d_j + +}{\partial d_j}. \end{aligned} \tag{35}$$

All of the terms in the right-hand side of (35) can be computed explicitly except $\frac{\partial \boldsymbol{\varepsilon}}{\partial d_j}$. We can expand $\frac{\partial \boldsymbol{\varepsilon}}{\partial d_j}$ as follows:

$$\frac{\partial \boldsymbol{\varepsilon}}{\partial d_j} \; [\;\; \Big) \frac{\partial \boldsymbol{\varepsilon}}{\partial \mathbf{x}^*} \frac{\partial \mathbf{x}^*}{\partial d_j} : \;\; \frac{\partial \boldsymbol{\varepsilon}}{\partial T} \frac{\partial T}{\partial d_j} : \;\; \frac{\partial \boldsymbol{\varepsilon}}{\partial C_f} \frac{\partial C_f}{\partial d_j} : \;\; \frac{\partial \boldsymbol{\varepsilon}}{\partial \alpha} \frac{\partial \alpha}{\partial d_j} \Big(, \tag{36}$$

where $\mathbf{x}^*$ is a column vector that only includes A_1^k, A_2^k, and ε_{z0}, and C_f is the concentration at the end of charging for concentric circle k, i.e. $C_f)r_k +$ All of the terms in (36) can explicitly be found except $\frac{\partial T}{\partial d_j}$ and $\frac{\partial \mathbf{x}^*}{\partial d_j}$. We used finite difference to compute $\frac{\partial T}{\partial d_j}$ term due to nonlinear nature of (14). To compute $\frac{\partial \mathbf{x}^*}{\partial d_j}$, we can take the derivative of (28) with respect to the design variable d_j as follows:

$$\frac{\partial \mathbf{A}}{\partial d_j}\mathbf{x} : \;\; \mathbf{A}\frac{\partial \mathbf{x}}{\partial d_j} \; [\;\; \frac{\partial \mathbf{b}}{\partial d_j}. \tag{37}$$

Note that $\frac{\partial \mathbf{x}^*}{\partial d_j}$ is actually part of column vector $\frac{\partial \mathbf{x}}{\partial d_j}$, which obtained for concentric circle k. We rearrange the terms in (37) as

$$\mathbf{A}\frac{\partial \mathbf{x}}{\partial d_j} \; [\;\; \frac{\partial \mathbf{b}}{\partial d_j} - \frac{\partial \mathbf{A}}{\partial d_j}\mathbf{x}. \tag{38}$$

Equation (38) can readily be solved for $\frac{\partial \mathbf{x}}{\partial d_j}$. Thus, we can find $\frac{\partial \mathbf{x}^*}{\partial d_j}$ and substitute it in (35) to calculate the sensitivity of stress with respect to the design parameter d_j. Note that we have verified the accuracy of our sensitivity analysis against the finite difference method.

3.2. Gradient-based design optimization under uncertainty

We extend the gradient-based design optimization scheme presented in section 3.1 to incorporate any sources of uncertainty. To do so, we integrate the non-intrusive polynomial chaos expansion (PCE) method into the proposed gradient-based scheme. We demonstrate our proposed scheme in the form of the reliability-based design optimization (RBDO) method. Let's consider a random variable vector $\boldsymbol{\xi} \; [\;\;)\xi_1, \ldots, \xi_{N_s} +$ which contains N_s random variables. Any response function $Y)\boldsymbol{\xi} +$ i.e. the objective function or constraints, can be expressed as a convergent series in terms of polynomials. This is due to our assumption on considering independent random variables with finite variance, which is applicable to most physical processes.

The PCE of $Y)\boldsymbol{\xi} +$ in a finite dimensional setting can be written as

$$Y)\boldsymbol{\xi} + \tilde{[} \prod_{i=0}^{N_c} r_i \psi_i)\boldsymbol{\xi} +, \tag{39}$$

where r_i is the PC coefficients, ψ_i is the polynomial basis functions, and $N_c : \;\; 1$ is the number of coefficients. The polynomial basis functions are selected such that they would be orthogonal with respect to the probability density functions of the random variables $\boldsymbol{\xi}$. Legendre polynomials are used in this study to satisfy the orthogonality criteria for the random variables [59]. Now that we know the form of basis

functions in (39), we need to find N_c and r_i. N_t [N_c : 1 is giving us the total number of coefficients in the PCE and it can be obtained from the following equation

$$N_t \left[1 : \prod_{v=1}^{p} \frac{1}{v\%}_{v=0}^{v-1})N_s : v+\left[\frac{)N_s : p+\%}{N_s\%p\%}, \right. \tag{40}$$

where N_s is the total number of random variables and p is the maximum order of polynomial ψ_i. To compute the coefficients r_i efficiently, we implement a non-intrusive method. The central idea in this approach is to find the value of response function Y at some smartly selected points, namely, quadrature points in the probability space of the underlying random variables.

Using the Galerkin projection method, we can obtain the coefficients as

$$r_i \left[\frac{E]Y\psi_i}{E]\psi_i^2}, \right. \tag{41}$$

where $E[.]$ is the mathematical expectation. The denominator of (41) can readily be computed since we know the form of the basis functions,

$$E]\psi_i^2 \left[\prod_{j=1}^{N_s} E]\psi_{i_j}^2 , \right. \tag{42}$$

where ψ_{i_j} is the univariate polynomial in each directions of ξ_j, j [$1, \ldots, N_s$. An analytical form for the numerator of (41) does not exist, hence, we estimate its value using the quadrature points, i.e.

$$E]Y\psi_i \left[\int_{\mathfrak{A}} Y)\boldsymbol{\xi}+\psi_i)\boldsymbol{\xi}+\rho)\boldsymbol{\xi}+d\boldsymbol{\xi} \backsimeq \prod_{q=1}^{n_q} Y)\boldsymbol{\xi}^{(q)}+\psi_i)\boldsymbol{\xi}^{(q)}+\omega^{(q)}, \right. \tag{43}$$

where $\boldsymbol{\xi}^{(q)}$ is the quadrature points, $\rho)\boldsymbol{\xi}+$is the probability density function of the independent random variable, $\omega^{(q)}$ is their respective weight, n_q is the number of quadrature points, and $\mathfrak{A}$ is the probability space. To efficiently selects the quadrature points, we use the Smolyak sparse grid construction, which is based on the one-dimensional Kronrod-Paterson quadrature [60, 61].

The idea in the RBDO scheme is to obtain a reliable design with a probability of failure under a predefined acceptable level. The RBDO formulation can be expressed as

$$\begin{aligned} &\min_{\mathbf{d}} E]\theta \ : \ \mathcal{C}_\theta \mathrm{Std}]\theta \ , \\ &\text{such that } =lb_j \leqslant d_j \leqslant ub_j, \quad j \left[1, 2, \ldots, n_d \right. \\ &P_f \left[P]g_i > 0 \ \leqslant \mathfrak{P} \quad j \right[1, 2, \ldots, n_g \end{aligned} \tag{44}$$

where C_θ is a constant determining the level of variability, Std is the standard deviation, n_g is the number of constraints, and $\mathfrak{P}$ is a constant demonstrating the level of reliability. P_f [$P]g_j > 0$ is the probability of failure and it can be defined as

$$P_f \left[P]g_j > 0 \left[\int_{\mathfrak{A}} H)g_j)\boldsymbol{\xi}+\rho)\boldsymbol{\xi}+d\boldsymbol{\xi}, \right. \right. \tag{45}$$

where H is the Heaviside function. Since the Heaviside function is not differentiable, we replace it with a continuous smooth approximation as follows:

$$P_f \left[\int_{\mathfrak{A}} \frac{1}{2} \right) \tanh \left) \frac{g_j)\boldsymbol{\xi}+}{\varepsilon} \right(: 1 \left(\rho)\boldsymbol{\xi}+d\boldsymbol{\xi}. \right. \tag{46}$$

where $\varepsilon > 0$ is a small number that controls the width of the 0 to 1 transition. We can compute (46) by Monte Carlo sampling on (39), i.e. $g_j)\boldsymbol{\xi}+[\sim \sum_{i=0}^{N_c} r_i\psi_i)\boldsymbol{\xi}+$ Thus, we have P_f [$\frac{n_{g_j>0}}{n_{\text{samples}}}$, where $n_{g_j>0}$ is the number of samples that satisfies $g_j > 0$ and n_{samples} is the number of Monte Carlo samples.

By Monte Carlo sampling on (39), the response function's mean and variance can readily be evaluated as

$$E]Y \left[\frac{1}{n_{\text{samples}}} \prod_{i=1}^{n_{\text{samples}}} Y)\boldsymbol{\xi}^{(i)}+, \right. \tag{47}$$

$$E\big]\big)Y-E\big]Y\big\}^2\Big(\Big[\ \frac{1}{n_{\text{samples}}}\prod_{i=1}^{n_{\text{samples}}}\big)Y\big)\boldsymbol{\xi}^{(i)}\big\}-E\big]Y\big\}^2, \tag{48}$$

where it is emphasized that these $Y\big)\boldsymbol{\xi}^{(i)}\big\}$realizations are efficiently obtained from the PCE of (39).

We also need to obtain the sensitivity of probabilistic measures such as means, variances, and failure probabilities. These can be evaluated by developing PCEs for sensitivities analogous to what we did for the random responses. The sensitivity of the response function with respect to the design parameters ($\boldsymbol{d}$) can be formulated as

$$\frac{\partial Y\big)\boldsymbol{\xi}\big\}}{\partial \boldsymbol{d}}\Big[\ \prod_{i=0}^{N}\boldsymbol{b}_i\psi_i\big)\boldsymbol{\xi}\big\}, \tag{49}$$

where

$$\boldsymbol{b}_i\Big[\ \frac{\partial r_i}{\partial \boldsymbol{d}}\Big[\ \frac{\sum_{q=1}^{N_q}\frac{\partial Y(\boldsymbol{\xi}^{(q)})}{\partial \boldsymbol{d}}\psi_i\big)\boldsymbol{\xi}^{(q)}\big\}w^{(q)}}{E\big]\psi_i^2}. \tag{50}$$

By means of Monte Carlo sampling on (49), the sensitivity of mean and variance with respect to the design parameters can be computed as

$$\frac{\partial E\big]Y}{\partial \boldsymbol{d}}\Big[\ \frac{1}{n_{\text{samples}}}\prod_{i=1}^{n_{\text{samples}}}\frac{\partial Y\Big)\boldsymbol{\xi}^{(i)}\Big(}{\partial \boldsymbol{d}}, \tag{51}$$

and

$$\frac{\partial E\big]\big)Y-E\big]Y\big\}^2\Big(}{\partial \boldsymbol{d}}\Big[\ \frac{2}{n_{\text{samples}}}\prod_{i=1}^{n_{\text{samples}}}\Big)\frac{\partial Y\Big)\boldsymbol{\xi}^{(i)}\Big(}{\partial \boldsymbol{d}}\Big(-\frac{\partial E\big]Y}{\partial \boldsymbol{d}}\Big(\sum\Big)Y\big)\boldsymbol{\xi}^{(i)}\big\}-E\big]Y\Big(, \tag{52}$$

where we should emphasize that the realizations $Y\big)\boldsymbol{\xi}^{(i)}\big\}$and $\partial Y\big)\boldsymbol{\xi}^{(i)}\big\}/\partial \boldsymbol{d}$ are efficiently computed from their PCE, equations (39) and (49).

The derivative of of the failure probability with respect to $\boldsymbol{d}$ is given by

$$\frac{\partial P_f}{\partial \boldsymbol{d}}\Big[\ \frac{1}{2\varepsilon n_{\text{samples}}}\prod_{i=1}^{n_{\text{samples}}}\frac{\partial g_j\Big)\boldsymbol{\xi}^{(i)}\Big(}{\partial \boldsymbol{d}}\Big(\Big)1-\tanh^2\Big)\frac{g_j\Big)\boldsymbol{\xi}^{(i)}\Big(}{\varepsilon}\Big(\Big(\Big(}{\sum\sum}. \tag{53}$$

Note that the non-intrusive PCE implementation is substantially facilitated via parallel processing due to the embarrassingly parallel nature of this method.

3.3. Bayesian optimization

In this study, we aim to use the Bayesian optimization (BO) scheme for the purpose of selecting the best materials for the constituents. BO is a global optimization method that attempts to minimize the objective function while satisfying constraints for bounded design space. The design parameters can be a combination of continuous and categorical parameters. BO keeps a Gaussian process model of the objective function, and train this model through the optimization process by smartly selecting new points in the design space to evaluate the objective function [48].

The design variables are polymer matrix material, carbon fiber material, the volume fraction of positive electrode particles, and the volume fraction of fibers. Thus, we have both continuous and categorical design parameters. The flowchart corresponding to this scheme is presented in figure 3. The optimizer constructs the Gaussian process model and uses an acquisition function to train it through the optimization process.

BO scheme is much simpler to implement in comparison with the gradient-based scheme presented in section 3.1. This is due to the fact that there is no need to perform sensitivity analysis since BO is a non-gradient optimization scheme. However, BO gets computationally expensive when it needs to deal with a problem that has many design parameters or many constraints.

4. Material properties and simulation parameters

For the base model, we considered IMS65 as the carbon fiber, poly(methoxy polyethylene glycol (350) monomethacrylate) as the coating, and AB/0.65 as the matrix which is reinforced with $LiFePO_4$ and CB particles. We approximate the electrochemical capacity ( ) of IMS65 carbon fiber and $LiFePO_4$ particles based on the experimental data in [62, 63] as

$$_{\mathrm{f}})C_{\mathrm{rate}}+\{\quad 0.18585-0.07419\ln)C_{\mathrm{rate}}+\ \text{for}\ \ C_{\mathrm{rate}}\in\,]0.08,6\ , \tag{54}$$

and

$$_{\mathrm{p}})C_{\mathrm{rate}}+\{\quad 0.1318-0.0112\ln)C_{\mathrm{rate}}+\ \text{for}\ \ C_{\mathrm{rate}}\in\,]0.08,6\ , \tag{55}$$

respectively.

Using the experimental data provided in [64], we estimate the modulus of elasticity of IMS65 in the longitudinal ($E_{z,f}$) and transverse ($E_{r,f}$) directions as

$$E_{z,f})C_{\mathrm{f}}+\{\quad 300)1-0.1126\ C_{\mathrm{f}}+, \tag{56}$$

and

$$E_{r,f})C_{\mathrm{f}}+\{\quad 30)1:\quad 1.5644\ C_{\mathrm{f}}+, \tag{57}$$

respectively. The temperature-dependent modulus of elasticity of polymer coating (E_{c}) and matrix (E_m) can be obtained based on the experimental observations in [50, 65]

$$E_{\mathrm{c}})T+\{\quad \begin{cases} 0.1)1-0.0533)T-25+, & \text{for}\ \ T\in\,]25,39 \\ 0.00133T^2-0.109T:\ \ 2.26, & \text{for}\ \ T\in\,]39,41 \\ 20, & \text{for}\ \ T\in\,]41,150 \end{cases} \tag{58}$$

$$E_m)T+\{\quad 2.95)10^{-5}+T^2-8.364)10^{-3}+T:\quad 0.765. \tag{59}$$

We estimate the ion-conductivities of the coating (s_c) and matrix (s_m) using the experimental data in [50]

$$s_c)T+\{\quad s_{c0})1:\quad 1.33)T-25+, \ \text{for}\ \ T\in\,]25,100\ , \tag{60}$$

$$s_m)T+\{\quad s_{m0})1:\quad 0.033)T-25+, \ \text{for}\ \ T\in\,]25,100\ , \tag{61}$$

where s_{m0} and s_{c0} are constants equal to $1.9(10^{-4})$ and $5(10^{-6})$, respectively.

Maximum possible concentration of lithium-ion inside a fiber (c_0) can be computed as

$$c_0\ [\quad \frac{_{\mathrm{f}})0.08+\rho_{\mathrm{f}}}{F}, \tag{62}$$

where ρ_{f} is the density of fiber. The rest of the material properties of the constituents for the reference model are listed in table 2. Simulation parameters for the reference model are also listed in table 3.

5. Results and discussion

In this section, we solve three numerical examples to demonstrate the capability of our proposed design optimization framework, and we provide discussions regarding the obtained results.

Table 2. Material properties of the reference model.

Parameter	Fiber	Coating	Matrix	$LiFePO_4$	CB	Reference
D_f ($m^2\ s^{-1}$)	10^{-14}	—	—	—	—	[24]
E_z (GPa)	Equation (56)	Equation (58)	Equation (59)	125	—	[23, 27, 50, 64, 65]
E_r (GPa)	Equation (57)	Equation (58)	Equation (59)	125	—	[23, 27, 50, 64, 65]
$\nu_{r\theta}$	0.45	0.3	0.3	0.28	—	[24, 27, 28]
ν_{zr}	0.2	0.3	0.3	0.28	—	[24, 27, 28]
β_z ($1/C_f$)	6.3×10^{-3}	—	—	—	—	[62, 66]
β_r ($1/C_f$)	3.2×10^{-2}	—	—	—	—	[62, 66]
$\mathfrak{f}$	0.5	—	—	0.5	0.12	—
ρ ($gr\ cm^{-3}$)	1.85	1	1	3.6	1.8	[31]
α_z ($1\ K^{-1}$)	-5.4×10^{-7}	2×10^{-5}	2×10^{-5}	10^{-5}	0	[67]
α_r ($1\ K^{-1}$)	10^{-5}	2×10^{-5}	2×10^{-5}	10^{-5}	0	[67]
c_p ($J\ grK^{-1}$)	0.71	1.67	1.67	0.45	0.71	[31]
s ($S\ cm^{-1}$)	690	Equation (60)	Equation (61)	—	7	[50, 68]
Γ ($Ah\ gr^{-1}$)	Equation (54)	—	—	Equation (55)	—	[62, 63]

Table 3. Simulation parameters for the reference model.

Parameter	r_f (μm)	δ_c (μm)	L(cm)	W(cm)	δ(cm)	C_{rate} ($1/h$)	T_{ref} (C)
Value	2.5	0.5	12	2.5	0.05	6	25

Table 4. Range of design parameters for Problem 1.

Design Parameter	L (cm)	W (cm)	δ (cm)	$\mathfrak{f}_f$	δ_c (μm)	$\mathfrak{f}_p$
Range	[4,20]	[1,4]	[0.01,0.1]	[0.3,0.7]	[0.1,0.5]	[0.3,0.7]

5.1. Problem 1: design of geometrical features of structural battery (deterministic gradient-based optimization approach)

We solve an illustrative example using a deterministic gradient-based design optimization scheme in this section. The objective is to maximize the allowable charging current for a constant rate of charging within the structural battery while three sets of inequality constraints are defined. First, we want the structural battery to be lightweight, so we impose a constraint on the maximum allowable mass for the structural battery. Second, we do not want the structural battery to overheat. Thus, a constraint is considered for the safe maximum temperature in the structural battery. Finally, we impose a set of constraints on the maximum acceptable value for stress components in the structural battery. Based on the application of structural battery and designer's decisions, these constraints values can be determined. As an illustrative example to show how our proposed scheme works, we select the constraints to be $m_{total} \leqslant 5$ gr, $T \leqslant 35\ ^\circ$C, and $|\sigma_i^{(k)}| \leqslant 40$ MPa, where m_{total} is the total mass of the structural battery and $\sigma_i^{(k)}$ is the ith component of stress (i.e. σ_r, σ_θ, and σ_z) in the concentric circle k. We need to emphasize that the proposed optimization method is general and the inequality constraints can be considered to be any value. For this problem, we select these values based on the recommended operating temperature for li-ion batteries, and the analysis performed in the previous studies [24, 31].

Six different design parameters are considered for this problem. Length (L), width (W), and thickness (δ) of structural battery lamina, fiber volume fraction ($\mathfrak{f}_f$), coating thickness (δ_c), and particle volume fraction ($\mathfrak{f}_p$). The ranges of these design parameters are defined based on the values used in the previous studies [22, 30, 31] (see table 4). Based on the convergence study on the required number of concentric circles for fiber, coating, and matrix presented in appendix B, we select 100 circles for fiber, 20 for coating, and 20 for matrix to conduct structural analysis.

Due to the non-convex nature of this problem, we create 20 random initial guesses and perform the optimization process for them to find the optimized design, as shown in figure 4. For this example, all of these twenty cases are converged to 0.997 (A). However, the optimized designs of them are different. As it is explained in [69], it is quite common in the gradient-based optimization methods to have the same objective value while the design parameters are different. Three cases out of these twenty cases are selected, and the history plots of their objective function as well as their constraints are presented in the inset plots in figure 4. Moreover, the values of their objective functions, their constraints, and their design parameters are listed in table 5 for both their reference and optimized designs.

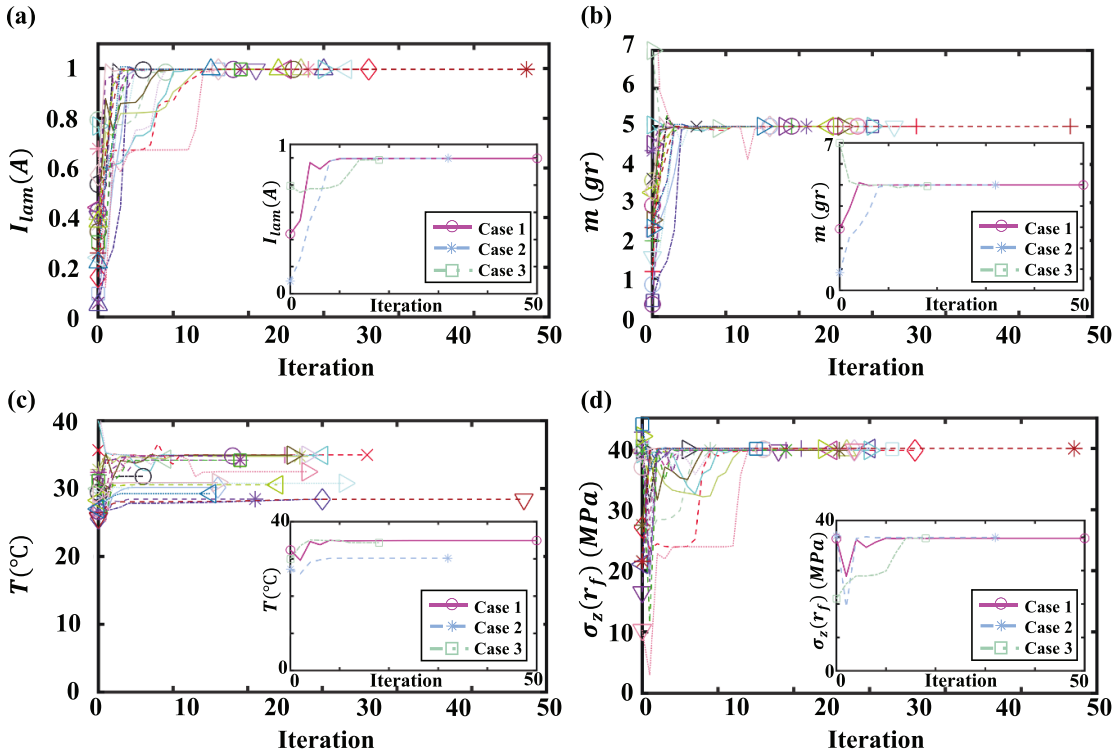

Figure 4. Evolution of (a) I_{lam}, (b) m, (c) T, and $\sigma_z(r_f)$ during the optimization process of Problem 1. The inset figures show the history plot of three selected cases out of twenty cases that the results of them are summarized in table 5.

Table 5. Results of three selected cases from twenty random initial designs for optimization Problem 1.

	Case 1		Case 2		Case 3	
	Reference	Optimized	Reference	Optimized	Reference	Optimized
I_{lam} (A)	0.441	0.997	0.094	0.997	0.574	0.997
m (gr)	2.92	5	0.84	5	5.57	5
T (°C)	32.38	34.92	27.23	30.17	27.43	34.71
σ_z (r_f)(MPa)	39.60	39.69	40.39	39.92	14.05	39.70
L (cm)	12	11.501	8	8.301	16	11.170
W (cm)	2.5	2.495	1.75	2.924	3.25	3.239
δ (cm)	0.05	0.0845	0.0325	0.1	0.0775	0.066
$\mathfrak{f}_{\text{f}}$	0.5	0.699	0.35	0.699	0.6	0.699
δ_c (μm)	0.3	0.1	0.325	0.1	0.5	0.1
$\mathfrak{f}_{\text{p}}$	0.5	0.7	0.35	0.7	0.6	0.699

To better understand the effect of each one of these design parameters on the values of objective function and constraints in our six-dimensional design space, we perform a sensitivity analysis in a statistical framework. Using Monte Carlo sampling, we select 1000 random points in our design space and we compute the sensitivity of objective function and constraints with respect to each design parameter.

Figure 5 shows the probability of having a positive, negative, and zero gradient for I_{lam}, m, T, and $\sigma_z)r_{\text{f}}+$ with respect to the design parameters L, W, δ, $\mathfrak{f}_{\text{f}}$, δ_{c}, and $\mathfrak{f}_{\text{p}}$. It can be seen that having a larger lamina (increasing L, W, and δ) results in rising the temperature, mass, and current, while it leads to a drop in the stress. This behavior is consistent with the observed results in [31]. We need to emphasize again that the optimizer wants to maximize the allowable charging current while there are constraints on the maximum possible values for mass, temperature, and stress. Thus, increasing the lamina size would be beneficial for maximizing the current and satisfying stress constraint, while it would have an adverse effect on satisfying the mass and temperature constraints.

An increase in the fiber volume fraction results in a drop in the total mass and stress as shown in figures 5(b) and (d). The reason for observing a reduction in the total mass by increasing the fiber volume fraction is explained in appendix C. Moreover, a rise in the fiber volume fraction, based on the values of the other parameters, may lead to either an increase or decrease in the current and temperature (see figures 5(a) and (c)). Note that an increase in the fiber volume fraction would rise the fiber mass (m_{f}) and decrease the

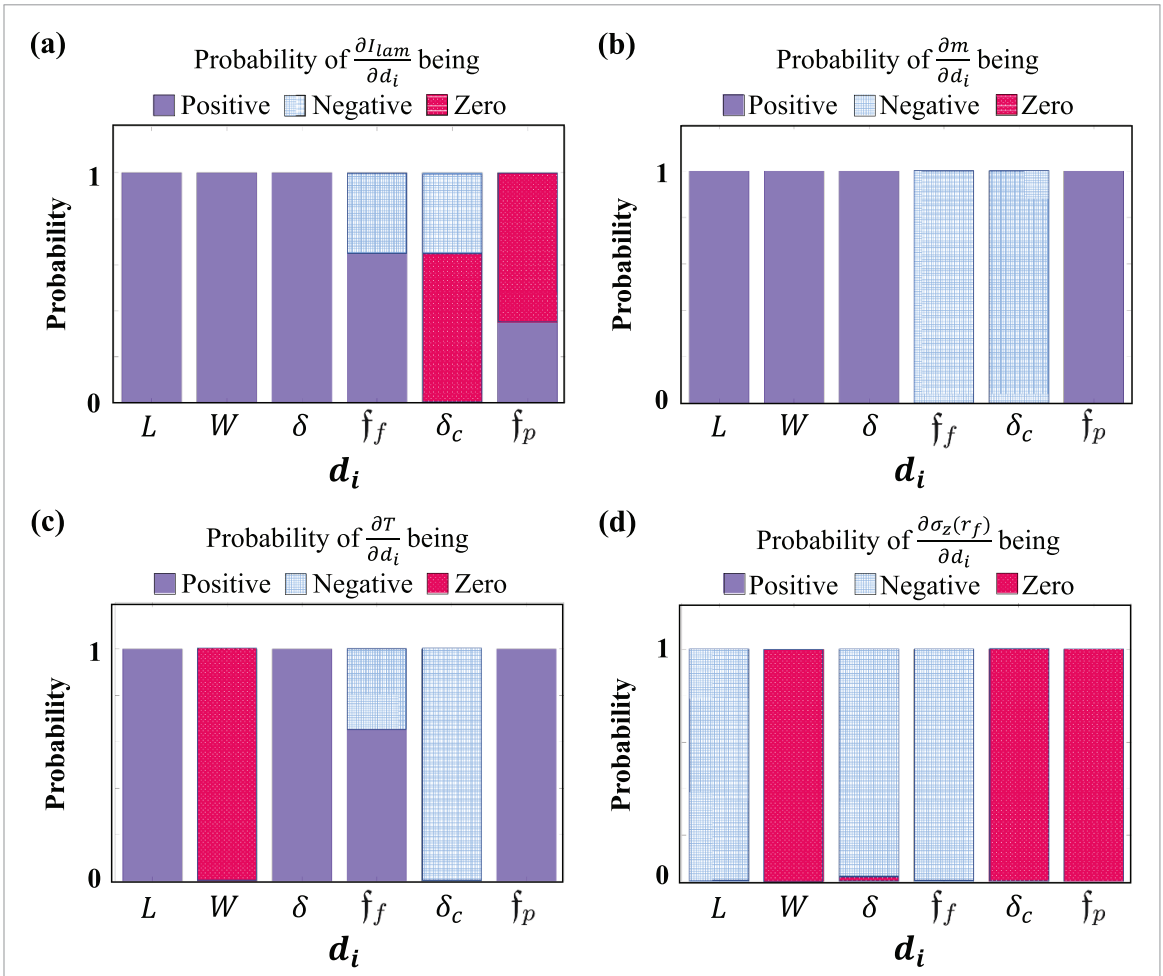

Figure 5. The probability of having a positive, negative, and zero gradient for (a) I_{lam}, (b) m, (c) T, and (d) $\sigma_z(r_f)$ with respect to the design parameters d_i for optimization Problem 1.

particle mass (m_p). Thus, based on the value of min) $_f m_f$, $_p m_f$ cf (5), the partial derivative of current with respect to the fiber volume fraction can be positive or negative. Consequently, the change in the fiber volume fraction may lead to either an increase or decrease in the temperature.

Coating thickness plays an important role in satisfying mass and temperature constraints. Indeed, increasing the coating thickness would result in decreasing both the mass and temperature of the lamina as shown in figures 5(b) and (c). But, a rise in the coating thickness might cause the current to decrease (see figure 5(a)). And finally, figures 5(b) and (c) demonstrate that a rise in particle volume fraction would increase total mass and temperature.

Thus, the conflicting behaviors explained in this section emphasizes the essence of performing a systematic design optimization approach to simultaneously satisfying all the constraints and maximizing the current[4].

5.2. Problem 2: design of structural battery under uncertainty (RBDO)

In this section, we optimize the design of a structural battery by using the RBDO scheme, and we compare the results with the deterministic (DET) approach to better understand the advantage of considering uncertainty in the optimization procedure. As an illustrative example, we consider uncertainty in the coating thickness (δ_c) and electrochemical capacity of particles ($_p$). We define an independent and uniform random variable $\boldsymbol{\xi}$ [ ) ξ_1, ξ_2 where ξ_1 [$0.1\delta_c$] $-1, 1$ and ξ_2 [0.1 $_p$] $-1, 1$. The base model of the structural battery presented in section 4 is considered as the reference design. In this optimization problem, we aim to maximize the allowable charging current for a constant rate of charging while three sets of inequality constraints are imposed to the optimization problem for the maximum allowable mass of 5 gr, temperature

[4] Note that the results provided in this section are based on the assumptions that we considered in our multi-physics model, and as explained in section 2, in the future, we aim to extend the proposed framework to incorporate a more comprehensive model.

Table 6. Optimized designs of Problem 2.

Scheme	L (cm)	W (cm)	δ (cm)	$\mathfrak{f}_f$	$\mathfrak{f}_p$
DET	14.66	2.49	0.065	0.519	0.7
RBDO	14.29	1.96	0.085	0.529	0.682

Table 7. The effect of changes made by the optimizer in the design variables of the optimized design of the RBDO scheme compared to the DET approach. The first row is the sign of change in the design variables from the optimized design of DET to the optimized design of RBDO schemes($\triangle d_i = d_{i,\text{RBDO}} - d_{i,\text{DET}}$).

	$\triangle L < 0$	$\triangle W < 0$	$\triangle \delta > 0$	$\triangle \mathfrak{f}_f > 0$	$\triangle \mathfrak{f}_p < 0$
m	+	+	−	+	+
T	+	0	−	±	+
$\sigma_z(r_f)$	−	0	+	+	0

+: Positive effect on satisfying the constraints.

−: Negative effect on satisfying the constraints.

0: No effect on satisfying the constraints.

±: Either positive or negative effect on satisfying the constraints.

of 35 °C, and stress of 20 MPa. The design parameters are L, W, δ, $\mathfrak{f}_f$, and $\mathfrak{f}_p$, and their ranges are similar to the ranges defined in table 4.

For the RBDO scheme, we use C_θ [0.1, and we consider the level of reliability to be at least 95%, i.e. $\mathfrak{P}$ [5(. We should emphasize that by 95% reliability, we mean that the optimized design should satisfy the prescribed constraints on the maximum allowable mass, temperature, and stress in the structural battery for at least 95% of the uncertainty scenarios. Without loss of generality, we select a polynomial of order 5 for our PCE construction. We also consider the number of Monte Carlo samples to be 10 000 to estimate the statistical moments of response functions. The values of the design parameters of the optimized designs obtained from DET and RBDO schemes are presented in table 6.

We compute the sign of change in the design variables from the optimized design of DET to the optimized design of RBDO schemes, as $\triangle d_i$ [$d_{i,\text{RBDO}} - d_{i,\text{DET}}$ to understand the decisions made by the optimizer to obtain a reliable design, i.e. a design that satisfies the prescribed constraints in the presence of uncertainty (see table 7). We then use the results of figure 5 to interpret whether this increase or decrease in the design variables is helpful or not for the optimizer to satisfy the constraints in the RBDO scheme. The results show that the optimizer needs to consider a trade-off between the changes that it wants to make in the design parameters to satisfy the constraints. For instance, the decrease in L is helpful to satisfy the constraints on m and T for the uncertainty scenarios, while it adversely affects the process of satisfying the stress constraint. An opposite behavior can be seen in the changes that the optimizer made in δ. An increase in δ helps the optimizer to satisfy the stress constraint while it is not helpful in satisfying the mass and temperature constraints.

Figure 6 compares the true probability density function (PDF)[5] of m, T, and $\sigma_z)r_f$+for the optimized designs of the DET and the RBDO schemes. As it is summarized in table 8, the optimized design of the RBDO scheme outperforms the optimized design of the DET optimization method in terms of having a smaller mean value, standard deviation, and probability of failure. The probability of failure in satisfying the mass, temperature, and stress constraints in the optimized design of DET is 51.65%, 50.47%, and 50.4%, respectively. By using the RBDO scheme, we obtained a reliable design, in which the probability of failure for all of the constraints is less than 5%.

5.3. Problem 3: design of constituents materials (Bayesian design optimization)

In the last problem, we aim to select the best materials for fibers and matrix from the pre-defined options to maximize the allowable charging current for a constant rate of charging and satisfy the imposed constraints. The constraints considered in this problem is exactly similar to the ones imposed in Problem 1. The design parameters are the material of the matrix, the material of fibers, the volume fractions of positive electrode particles, and the volume fraction of fibers.

[5] True PDF is plotted using *ksdensity* function in MATLAB for all 10^4 uncertainty scenarios. The PDF can be defined as $\hat{f}(a) = \frac{1}{nh}\sum_{j=1}^{n} K\left(\frac{a-a_j}{h}\right)$, where n is the number of data points, h is the bandwidth, a is the variable that we want to find its PDF, and $K(.)$ is the kernel smoothing function.

Table 8. Summary of the statistical analysis results of Problem 2.

Metric	Scheme	E	Std	P_f
m	DET	5	0.036	51.65
	RBDO	4.94	0.035	2.73
T	DET	35.06	1.257	50.47
	RBDO	33.24	1.039	5
$\sigma_z(r_f)$	DET	20	1.112	50.40
	RBDO	18.13	1.080	3.99

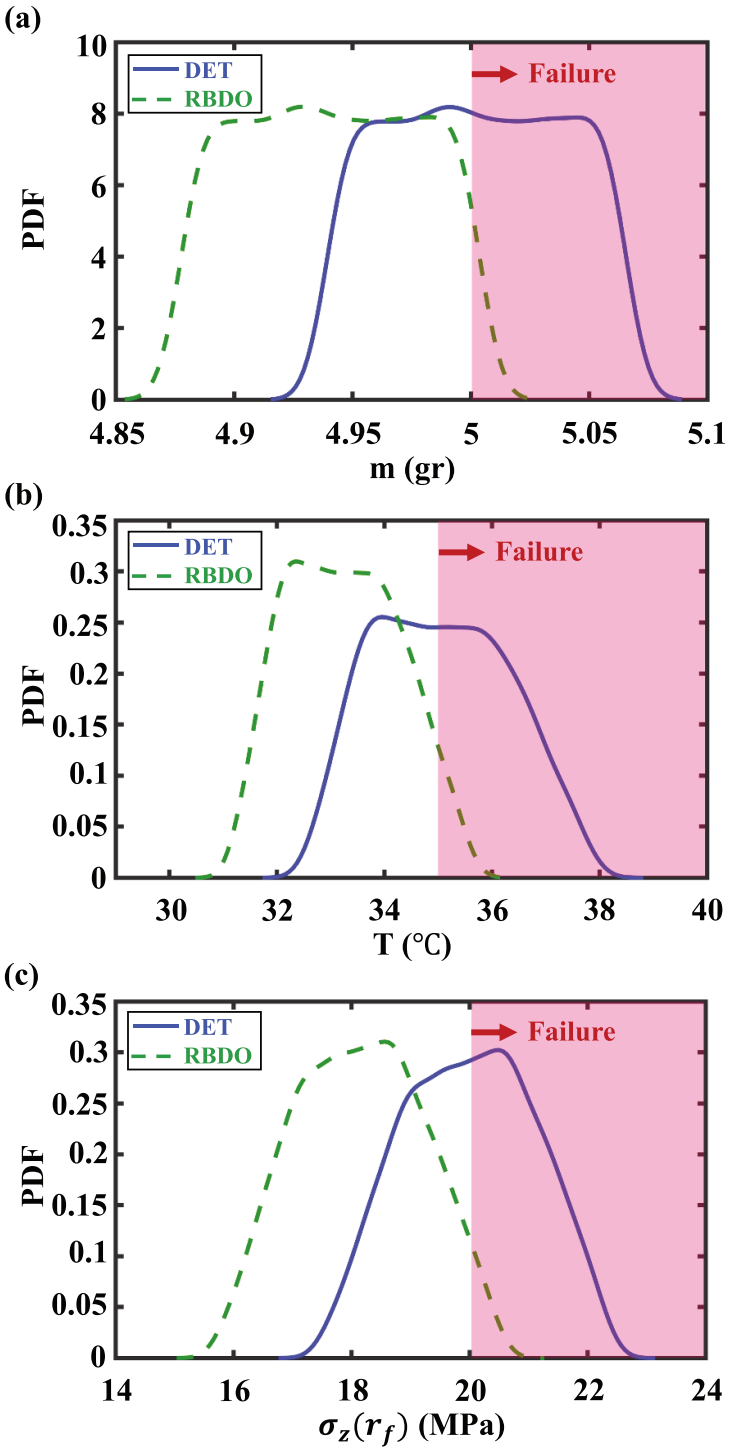

Figure 6. True PDF of (a) m, (b) T, and (c) $\sigma_z(r_f)$ for the optimized designs of DET and RBDO schemes used for Problem 2. The failure region, in which the constraint is violated, is indicated with the red shaded area.

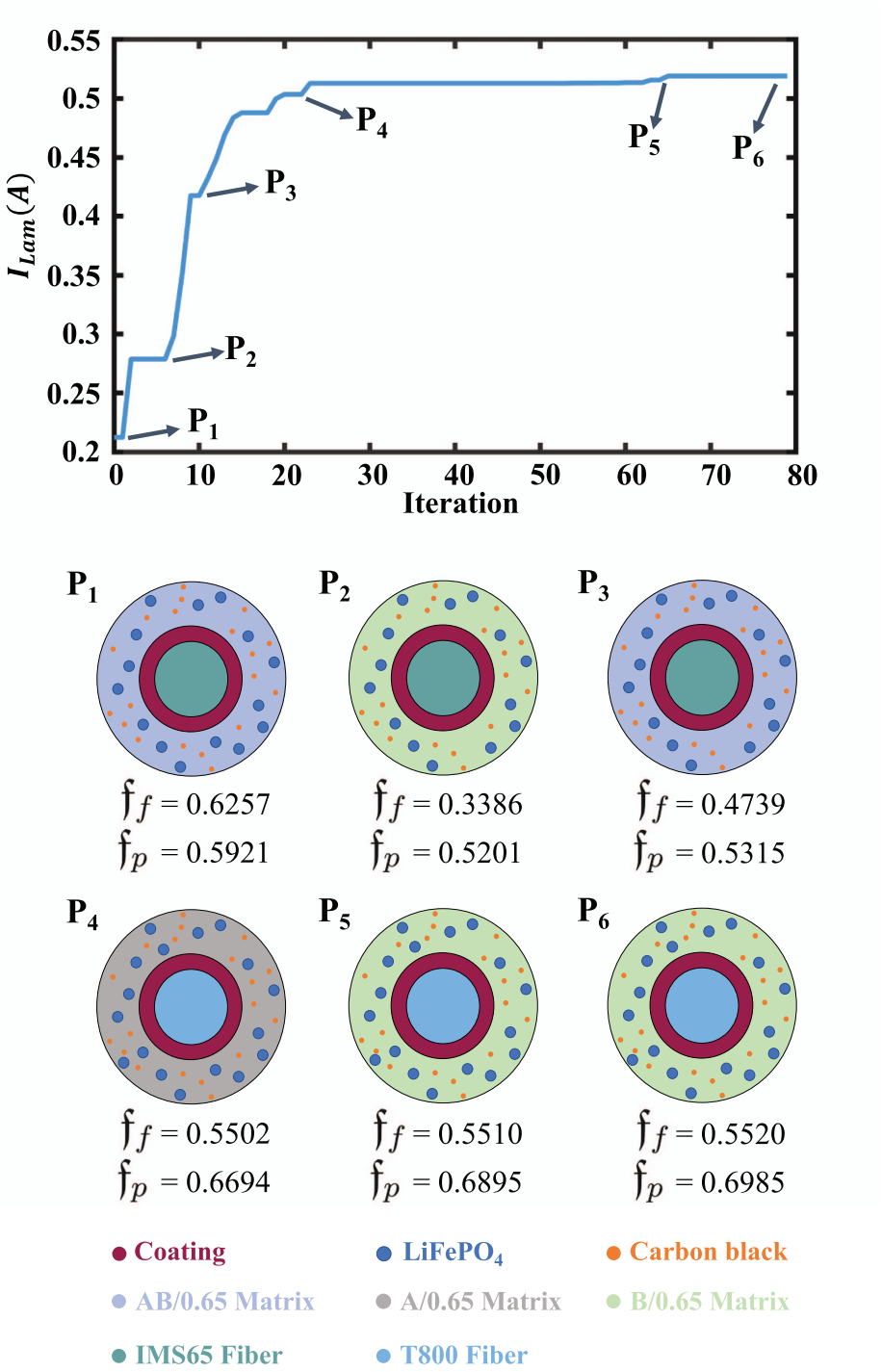

Figure 7. History Plot of the objective function of optimization Problem 3. The material types and design parameter values of 6 indicated points in the history plot (i.e. points $\mathbf{P}_1$–$\mathbf{P}_6$) is also shown in the figure. The colors indicate the materials selected by the optimizer.

Three types of common materials for polymer matrix in a structural battery, as explained in table 1, are selected as the options for matrix material. These materials are named A/0.65, B/0.65, and AB/0.65. The material properties of AB/0.65 are presented in section 4. The ion conductivity of material A/0.65 and B/0.65 can be approximated by (61) while using s_{m0} equal to $2.1(10^{-4})$ and $2(10^{-4})$, respectively [50]. Moreover, the temperature-dependent modulus of elasticity can be approximated for material A/0.65 by $E_m)T+[\ \ 2.78$ $)10^{-5}+T^2-6.768)10^{-3}+T:\ \ 0.701$ and for material B/0.65 by $E_m)T+[\ \ 4.55)10^{-5}+T^2-10.541)10^{-3}+T$ $:\ 0.608$ [50].

We consider two different types of carbon fibers (T800 and IMS65) as the options for fiber materials. The material properties of IMS65 are presented in section 4. The electrochemical capacity of T800 can be approximated by $_{\mathrm{f}})C_{\mathrm{rate}}+[\ \ 0.21366-0.07729\ \ln)C_{\mathrm{rate}}+$ for $C_{\mathrm{rate}} \in]0.08,6$ [62]. The density, heat

capacity, and longitudinal thermal expansion coefficients are 1.8 gr cm^{-3}, 0.75 (J grK^{-1}), and $-5.6(10^{-7})$ (K^{-1}), respectively [70]. The ion conductivity of T800 is 714 (S cm^{-1}) [68]. For the fiber and particle volume fractions, we assume a lower bound of 0.3 and an upper bound of 0.7 in the design space.

The history plot of the optimization Problem 3 is shown in figure 7. The optimizer selects T800 as the material for fiber, B/0.65 as the material for matrix, fiber volume fraction equal to $\mathfrak{f}_f$ [0.552, and particle volume fraction equal to $\mathfrak{f}_p$ [0.6985. We have selected six different points on the history plot, and their corresponding design parameters are shown in figure 7.

The main reason that the optimizer prefers T800 over IMS65 for the carbon fiber is that for this problem using T800 leads to an increase in the objective function (i.e. the allowable charging current). To explain this behavior, we need to emphasize that for a constant C_{rate}, the current is only correlated to min{ $_fm_f$, $_pm_p$}, i.e. $I_{lam} \propto$ min{ $_fm_f$, $_pm_p$}, cf (5). For the obtained volume fractions of fiber and particles in the optimized solution, the value of min{ $_fm_f$, $_pm_p$} for the cases that T800 and IMS65 are selected as the material for fiber is $_pm_p$ and $_fm_f$, respectively[6]. Since $_pm_p$ is larger than $_fm_f$ of IMS65, the maximum value of the current occurs when the optimizer selects T800 as the fiber material.

6. Conclusions

The structural battery is a new class of multifunctional materials that can harvest electrical energy while providing mechanical integrity. These materials are in their early stages of development, and there is an absolute need in the literature to provide design optimization frameworks for them to enhance their capability and effectiveness. In this study, we present a multi-physics design optimization framework to maximize the allowable charging current for a constant rate of charging in a structural battery by changing the geometrical features and material types of the constituents in a composite lamina. In this optimization framework, three sets of inequality constraints are defined to keep the structural battery lightweight, and make sure that the amount of induced stress and generated heat due to the intercalation process remains small. This framework contains a gradient-based design optimization scheme, which can perform the optimization process under any source of uncertainty, as well as the Bayesian design optimization method aimed to select the best candidate for the materials of the constituents in a structural battery. We employ the non-intrusive polynomial chaos expansion (PCE) approach to quantify the uncertainty propagation. This method facilitates the inclusion of almost any source of uncertainty in the design optimization process.

Design is an iterative process and often requires a simplified or reduced-order model to decrease the computational burden. In particular, in this study, we need to perform a transient analysis on a multi-physics problem which is a costly problem to solve. Thus, to reduce the computational burden, we take advantage of a simplified and efficient semi-analytical model. To build our design optimization scheme, we develop an analytical sensitivity analysis of several response metrics with respect to the considered design variables. Moreover, for the uncertainty quantification, the non-intrusive PCE allows for using of parallel processing due to its embarrassingly parallel nature leading to a reduction in the computational cost. The most important findings of the study have been listed in the following points:

- The presented design optimization framework enables us to optimize the geometrical features of a structural battery lamina as well as the material types of the constituents based on the applications and the design's requirements.
- Using the developed sensitivity analysis in the statistical framework, we investigate the effect of the considered design parameters in this study such as geometrical features of the composite lamina and volume fractions of fibers and $LiFePO_4$ particles on the considered response metrics including current, temperature, mass, and stress.
- The results reveal that for the considered design space in the problem solved in this study, having a larger composite lamina leads to an increase in the temperature, mass, and current, while it results in a drop in the stress.
- By performing optimization under uncertainty, we increase the reliability of the optimized design, i.e. the probability of satisfying the prescribed constraints in the presence of uncertainty, by at least 45% in comparison with the deterministic optimized design.

[6] Note that for the optimized solution the mass of fiber is $m_f = 1.5318$ gr and the particle mass is $m_p = 0.7737$ gr. Moreover, for $C_{rate} = 6\ (1/h)$, we obtain $\Gamma_f = 0.0752$ (Ah/gr) for T800, $\Gamma_f = 0.0529$ (Ah/gr) for IMS65, and $\Gamma_p = 0.1118$ (Ah/gr).

Acknowledgments

The authors acknowledge the financial supports by a 2019 Career Development and a 2020 Faculty Summer Research awards (Grant No. 284094) as well as the high-performance computing resources (PROTEUS: the Drexel Cluster) at Drexel University. The authors would also like to thank the National Science Foundation (Grant No. 2034108) for supporting this work.

Conflict of interest

There are no conflict of interests to declare.

Appendix A

We verify the analysis module used in this study by comparing the displacement and stress components obtained from our Semi-Analytical Framework with a finite element model set up in COMSOL [71]. To do so, we consider the base model introduced in section 4, and we create a 2D axisymmetric model in COMSOL. The displacement along the symmetric axis is assumed to be zero, and the external surface is considered to be free. The lithium concentration in the fiber is approximated by using a 1D axisymmetric diffusion model, providing input to the structural module. The temperature change within the domain is computed using (14), providing inputs for calculating the thermal strains. The generalized plane strain is assumed for this problem, and the displacement and stress distribution is obtained at the end of the charging step. Figure A1 demonstrates the comparison between the Semi-Analytical Framework and COMSOL. We observe a perfect agreement between the results confirming the accuracy of our analysis module.

Note that as we mentioned in section 3.1, we have verified the accuracy of the gradient-based optimization scheme used in this study by comparing the developed analytic sensitivity analysis against finite-difference. We have also performed the optimization process from different initial designs to make sure that the produced solutions are indeed optimized. Since the structural battery is a new concept and still in the early stages of development, we currently do not have the capability to perform an experimental validation for the proposed solutions, and we aim to extend our framework to incorporate experimental validation in future studies.

Appendix B

To find the appropriate number of concentric circles for fiber, coating, and matrix, we perform a convergence study using the material properties and simulation parameters of the base model presented in section 4 as it is shown in figure B2. Based on the results, we select 100 circles for fiber, 20 for coating, and 20 for matrix. Note that in this convergence study, r_f [2.5 μm, δ_c [$r_c - r_f$ [0.5 μm, and δ_m [$r_m - r_c$ [$r_f/\sqrt{f_f} - r_c \approx 0.5$ μm. Since the radius of fiber is five times larger than the thickness of coating and matrix, we considered the number of circles in the fiber to be five times larger than the ones in the coating and matrix in our convergence study to have uniformly spaced circles in the cell.

Appendix C

In this section, we mathematically prove that an increase in the fiber volume fraction in the considered design space in Problem 1 of section 5.1 leads to a decrease in the total mass. We can compute the total mass (m_{tot}) as follows:

$$m_{tot} [\rho_f V_f : \rho_c V_c : \rho_m V_m : \rho_p V_p : \rho_{cb} V_{cb}, \tag{C.1}$$

where ρ_f, ρ_c, ρ_m , ρ_p, ρ_{cb} are the densities of fiber, coating, matrix, $LiFePO_4$ particles, and carbon black particles, respectively. V_f, V_c, V_m , V_p, V_{cb} are the volumes of fiber, coating, matrix, $LiFePO_4$ particles, and carbon black particles, respectively.

Equation (C.1) can be expanded as

$$\begin{aligned} m_{tot} [\; & \rho_f f_f V_{tot} : \rho_c \pi) r_c^2 - r_f^2 + L : \rho_m) 1 - f_f + 1 - f_p - f_{cb} + V_{tot} : \rho_p) f_p + 1 - f_f + V_{tot} \\ & : \rho_{cb}) f_{cb} + 1 - f_f + V_{tot}, \end{aligned} \tag{C.2}$$

where f_{cb} is the volume fraction of carbon black within the matrix and V_{tot} is the total volume of lamina.

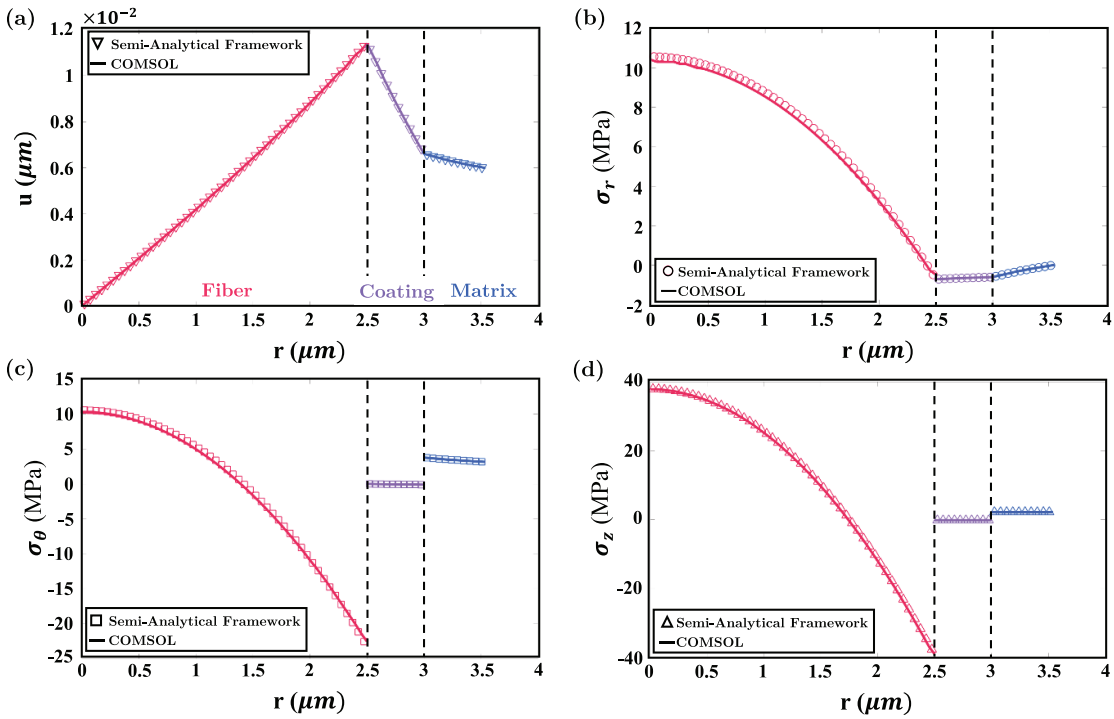

Figure A1. Verification of analysis module by comparison with COMSOL for (a) displacement, (b) radial stress, (c) hoop stress, and (d) longitudinal stress.

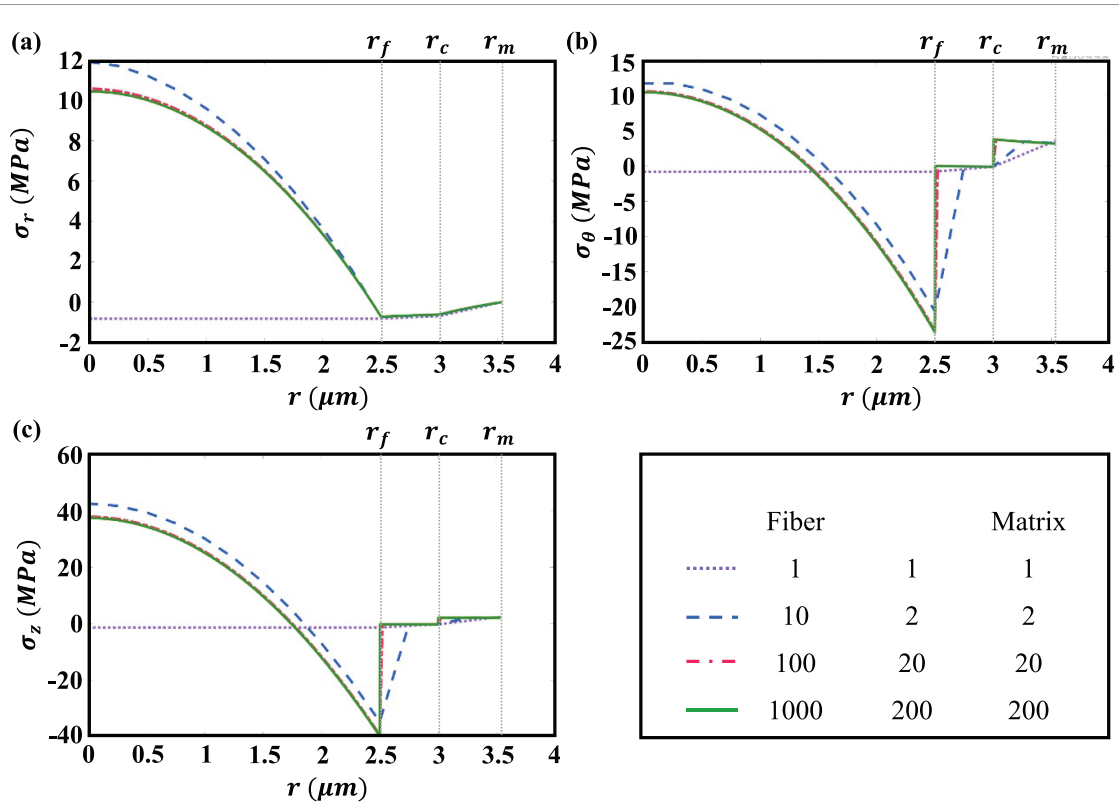

Figure B2. Convergence study to obtain the appropriate number of concentric circles in each constituents.

The partial derivative of (C.2) with respect to f_f is given by

$$\frac{\partial m_{tot}}{\partial f_f}[\ \rho_f V_{tot}:\ \rho_m)-1:\ f_p:\ f_{cb}+V_{tot}-\rho_p)f_p+V_{tot}-\rho_{cb})f_{cb}+V_{tot}. \tag{C.3}$$

We can readily show that for the given material properties and simulation parameters in section 4, (C.3) reduces to $)0.754 - 2.6\mathfrak{f}_p + WL\delta$. Hence, for $\mathfrak{f}_p > 0.29$, $\frac{\partial m}{\partial \mathfrak{f}_f}$ will be a negative number. Since we considered $\mathfrak{f}_p \in]0.3, 0.7$ in our design space, we observe that an increase in fiber volume fraction would lead to a drop in the mass.

ORCID iDs

Reza Pejman https://orcid.org/0000-0001-6405-2721
Emin Caglan Kumbur https://orcid.org/0000-0002-2363-7560
Ahmad Raeisi Najafi https://orcid.org/0000-0001-5432-9440

References

[1] Sprague R 2015 An analysis of current battery technology and electric vehicles *J. Undergrad. Res.* **8** 70–5
[2] Greenhalgh E S 2011 Storage solutions *Mater. World* **19** 24–6
[3] Snyder J F, O'Brien D J, Baechle D M, Mattson D E and Wetzel E D 2008 Structural composite capacitors, supercapacitors, and batteries for US Army Applications 43314
[4] Christodoulou L and Venables J D 2003 Multifunctional material systems: the first generation *JOM* **55** 39–45
[5] Gibson R F 2010 A review of recent research on mechanics of multifunctional composite materials and structures *Compos. Struct.* **92** 2793–2810
[6] Pejman R, Maghami E and Najafi A R 2020 How to design a blockage-tolerant cooling network? *Appl. Therm. Eng.* **181** 115916
[7] Pety S J, Tan M H Y, Najafi A R, Barnett P R, Geubelle P H and White S R 2017 Carbon fiber composites with 2D microvascular networks for battery cooling *Int. J. Heat Mass Transfer* **115** 513–22
[8] Tan M H Y, Najafi A R, Pety S J, White S R and Geubelle P H 2016 Gradient-based design of actively-cooled microvascular composite panels *Int. J. Heat Mass Transfer* **103** 594–606
[9] Pejman R and Najafi A R 2020 Network redundancy: a key design factor for cooling networks *ASME 2020 Int. Design Engineering Technical Conferences and Computers and Information in Conf.* (American Society of Mechanical Engineers Digital Collection) (https://doi.org/10.1115/DETC2020-22107)
[10] Tan M H Y, Najafi A R, Pety S J, White S R and Geubelle P H 2018 Multi-objective design of microvascular panels for battery cooling applications *Appl. Therm. Eng.* **135** 145–57
[11] Pety S J, Tan M H Y, Najafi A R, Gendusa A C, Barnett P R, Geubelle P H and White S R 2018 Design of redundant microvascular cooling networks for blockage tolerance *Appl. Therm. Eng.* **131** 965–76
[12] Johannisson W, Zenkert D and Lindbergh G 2019 Model of a structural battery and its potential for system level mass savings *Multifunct. Mater.* **2** 035002
[13] Wetzel E D 2004 Reducing weight: multifunctional composites integrate power, communications and structure *AMPTIAC Q.* **8** 91–5
[14] Snyder J F, Baechle D M, ED Wetzel and Xu K 2008 Multifunctional structural composite batteries for US army applications Technical report Army Research Lab Aberdeen Proving Ground Md
[15] Wong E L, Baechle D M, Xu K, Carter R H, Snyder J F and Wetzel E D 2007 Design and processing of structural composite batteries Technical report Army Research Lab Aberdeen Proving Ground MD
[16] Snyder J F, Carter R H and Wetzel E D 2007 Electrochemical and mechanical behavior in mechanically robust solid polymer electrolytes for use in multifunctional structural batteries *Chem. Mater.* **19** 3793–801
[17] Liu P, Sherman E and Jacobsen A 2009 Design and fabrication of multifunctional structural batteries *J. Power Sources* **189** 646–50
[18] Ekstedt S 2010 Maciej Wysocki and LE Asp. structural batteries made from fibre reinforced composites *Plast. Rubber Compos.* **39** 148–50
[19] Leif A S P, Bismarck A, Lindberg G, Leijonmarck S, Carlson T and Kjell M 2015 Battery half cell, a battery and their manufacture US Patent App. 14/634,932
[20] Asp L E and Greenhalgh E S 2014 Structural power composites *Compos. Sci. Technol.* **101** 41–61
[21] Lee C, Greenhalgh E S, Shaffer M S P and Panesar A 2019 Optimized microstructures for multifunctional structural electrolytes *Multifunct. Mater.* **2** 045001
[22] Carlstedt D and Asp L E 2020 Performance analysis framework for structural battery composites in electric vehicles *Composites* B **186** 107822
[23] Johanna X, Lindbergh G and Varna J 2018 Multiphysics modeling of mechanical and electrochemical phenomena in structural composites for energy storage: single carbon fiber micro-battery *J. Reinf. Plast. Compos.* **37** 701–15
[24] Johanna X, Lindbergh G and Varna J 2018 Carbon fiber composites with battery function: stresses and dimensional changes due to Li-ion diffusion *J. Compos. Mater.* **52** 2729–42
[25] Dionisi F, Harnden R and Zenkert D 2017 A model to analyse deformations and stresses in structural batteries due to electrode expansions *Compos. Struct.* **179** 580–9
[26] Carlstedt D, Runesson K, Larsson F, Johanna X and Asp L E 2020 Electro-chemo-mechanically coupled computational modelling of structural batteries *Multifunct. Mater.* **3** 045002
[27] Johanna X and Varna J 2020 Matrix and interface cracking in cross-ply composite structural battery under combined electrochemical and mechanical loading *Compos. Sci. Technol.* **186** 107891
[28] Pupurs A and Varna J 2014 Modeling mechanical stress and exfoliation damage in carbon fiber electrodes subjected to cyclic intercalation/deintercalation of lithium ions *Composites* B **65** 69–79
[29] Johanna X and Varna J 2019 Matrix and interface microcracking in carbon fiber/polymer structural micro-battery *J. Compos. Mater.* **53** 3615–28
[30] Carlstedt D, Marklund E and Asp L E 2019 Effects of state of charge on elastic properties of 3D structural battery composites *Compos. Sci. Technol.* **169** 26–33
[31] Carlstedt D and Asp L E 2019 Thermal and diffusion induced stresses in a structural battery under galvanostatic cycling *Compos. Sci. Technol.* **179** 69–78

[32] Asp L E and Greenhalgh E S 2015 Multifunctional structural battery and supercapacitor composites *Multifunct. Polym. Compos.-Challenges New Solut.* 619–61
[33] Najafi A R, Safdari M, Tortorelli D A and Geubelle P H 2017 Shape optimization using a NURBS-based interface-enriched generalized FEM *Int. J. Numer. Methods Eng.* **111** 927–54
[34] Najafi A R, Safdari M, Tortorelli D A and Geubelle P H 2015 A gradient-based shape optimization scheme using an interface-enriched generalized FEM *Comput. Methods Appl. Mech. Eng.* **296** 1–17
[35] Bendsoe M P and Sigmund O 2013 *Topology Optimization: Theory, Methods and Applications* (Berlin: Springer)
[36] Bendsøe M P and Sigmund O 1999 Material interpolation schemes in topology optimization *Arch. Appl. Mech.* **69** 635–54
[37] Thoft-Cristensen P and Baker M J 2012 *Structural Reliability Theory and its Applications* (Berlin: Springer)
[38] Boyle P P 1977 Options: a Monte Carlo approach *J. Financ. Econ.* **4** 323–38
[39] Melchers R E 1989 Importance sampling in structural systems *Struct. saf.* **6** 3–10
[40] Makarovic B 1973 Progressive sampling for digital terrain models *ITC J.* **3** 397–416
[41] Bucher C G 1988 Adaptive sampling—an iterative fast Monte Carlo procedure *Struct. saf.* **5** 119–26
[42] Hasofer A M and Lind N C 1974 Exact and invariant second-moment code format *J. Eng. Mech. Div.* **100** 111–21
[43] Fiessler B, Rackwitz R and Neumann H-J 1979 Quadratic limit states in structural reliability *J.e Eng. Mech. Div.* **105** 661–76
[44] Shinozuka M and Deodatis G 1988 Response variability of stochastic finite element systems *J. Eng. Mech.* **114** 499–519
[45] Yamazaki F, Shinozuka M and Dasgupta G 1988 Neumann expansion for stochastic finite element analysis *J. Eng. Mech.* **114** 1335–54
[46] Ghanem R G and Spanos P D 2003 *Stochastic Finite Elements: A Spectral Approach* (Chelmsford, MA: Courier)
[47] Pejman R, Keshavarzzadeh V and Najafi A R 2021 Hybrid topology/shape optimization under uncertainty for actively-cooled nature-inspired microvascular composites *Comput. Methods Appl. Mech. Eng.* **375** 113624
[48] MATLAB version 8.5 (R2015a) The MathWorks Inc. Natick, MA 2015
[49] Leijonmarck S, Carlson T, Lindbergh G, Asp L E, Maples H and Bismarck A 2013 Solid polymer electrolyte-coated carbon fibres for structural and novel micro batteries *Compos. Sci. Technol.* **89** 149–57
[50] Ihrner N, Johannisson W, Sieland F, Zenkert D and Johansson M 2017 Structural lithium ion battery electrolytes via reaction induced phase-separation *J. Mater. Chem.* A **5** 25652–9
[51] Jacques E, Kjell M, Zenkert D, Lindbergh G and Behm M 2011 Impact of mechanical loading on the electrochemical behaviour of carbon fibers for use in energy storage composite materials *18th Int. Conf. on Composites Materials, ICCM 2011* (*Jeju, 21 August 2011 Through 26 August 2011*)
[52] Verbrugge M W and Koch B J 1999 Electrochemistry of intercalation materials charge-transfer reaction and intercalate diffusion in porous electrodes *J. Electrochem. Soc.* **146** 833
[53] Verbrugge M W and Koch B J 1996 Modeling lithium intercalation of single-fiber carbon microelectrodes *J. Electrochem. Soc.* **143** 600
[54] Crank J 1979 *The Mathematics of Diffusion* (Oxford: Oxford University Press)
[55] Marklund E and Varna J 2009 Modeling the hygroexpansion of aligned wood fiber composites *Compos. Sci. Technol.* **69** 1108–14
[56] Sadd M H 2009 *Elasticity: Theory, Applications and Numerics* (New York: Academic)
[57] Hashin Z 1983 Analysis of composite materials—a survey
[58] Christensen R M 2012 *Mechanics of Composite Materials* (Chelmsford, MA: Courier)
[59] Xiu D and Karniadakis G E 2002 The Wiener–Askey polynomial chaos for stochastic differential equations *SIAM J. Sci. Comput.* **24** 619–44
[60] Kronrod A S 1965 Nodes and weights of quadrature formulas: sixteen-place tables
[61] Patterson T N L 1968 The optimum addition of points to quadrature formulae *Math. Comput.* **22** 847–56
[62] Jacques E, Kjell M H, Zenkert D, Lindbergh G and Behm M 2013 Expansion of carbon fibres induced by lithium intercalation for structural electrode applications *Carbon* **59** 246–54
[63] Zhang W-J 2010 Comparison of the rate capacities of $LiFePo_4$ cathode materials *J. Electrochem. Soc.* **157** A1040
[64] Yue Q, Guo H, Hector Jr L G and Timmons A 2010 Threefold increase in the Young's modulus of graphite negative electrode during lithium intercalation *J. Electrochem. Soc.* **157** A558
[65] Willgert M, Kjell M H, Lindbergh G and Johansson M 2013 New structural lithium battery electrolytes using thiol–ene chemistry *Solid State Ion.* **236** 22–9
[66] Yue Q, Hector Jr L G, James C and Kim K J 2014 Lithium concentration dependent elastic properties of battery electrode materials from first principles calculations *J. Electrochem. Soc.* **161** F3010
[67] Bowles D E and Tompkins S S 1989 Prediction of coefficients of thermal expansion for unidirectional composites *J. Compos. Mater.* **23** 370–88
[68] Kjell M H, Jacques E, Zenkert D, Behm M and Lindbergh G 2011 Pan-based carbon fiber negative electrodes for structural lithium-ion batteries *J. Electrochem. Soc.* **158** A1455
[69] Pejman R, Aboubakr S H, Martin W H, Devi U, Tan M H Y, Patrick J F and Najafi A R 2019 Gradient-based hybrid topology/shape optimization of bioinspired microvascular composites *Int. J. Heat Mass Transfer* **144** 118606
[70] (Available at: www.cncarbonfiber.com/)
[71] *COMSOL Multiphysics*. v. 5.6., COMSOL AB, Stockholm, Sweden (available at: www.comsol.com)